Journal of Aerosol Science 189 (2025) 106634

Contents lists available at ScienceDirect

Journal of Aerosol Science

journal homepage: www.elsevier.com/locate/jaerosci

In-vitro visualization of aerosol deposition by laser-induced fluorescence in a human airway model

Stefanie Gürzing [a,*], Anja Lena Thiebes [b], Christian Gabriel Cornelissen [b,c], Stefan Jockenhoevel [b], Manuel Reddemann [a]

[a] *Institute of Heat and Mass Transfer, RWTH Aachen University, Aachen, Germany*
[b] *Department of Biohybrid and Medical Textiles (BioTex), AME—Institute of Applied Medical Engineering, Helmholtz Institute Aachen, RWTH Aachen University, Aachen, Germany*
[c] *Department of Pneumology and Internal Intensive Care Medicine, Medical Clinic V, University Hospital Aachen, RWTH Aachen University, Aachen, Germany*

ARTICLE INFO

Keywords:
Human lung
Aerosol deposition
Experimental airway model
Deposition mechanism
Laser-induced fluorescence

ABSTRACT

This study presents the first *in-vitro* visualization of aerosol deposition from the trachea up to the 10th bifurcation in a transparent airway model. The airway model simulates a representative respiratory tract of the left lower lobe and consists of all 23 generations of a human lung. Laser-induced fluorescence (LIF) was used to investigate the temporal and spatial deposition behavior of aerosols generated by a jet nebulizer along the representative airway. The *in-situ* measured LIF signal correlates to the amount of deposited aerosol during spontaneous breathing. By the means of LIF-image post-processing the temporal course of the LIF signal in each of the first eight bifurcations is correlated to the main aerosol deposition mechanisms, i.e. inertial impaction and gravitational settling, in the conductive airways. Depending on the time point in the respiratory cycle either one of both deposition mechanisms dominates the current aerosol deposition. The spatial analysis over eight subsequent bifurcations shows the diminishing influence of the inertial deposition mechanism over deeper bifurcations. Further, the duration of gravitational settling decreases over the bifurcations depending on the accompanying airway diameters of each bifurcation. The introduction of the dimensionless Froude number allows the comparison of the measured aerosol deposition to existing research and demonstrates that the proposed threshold limit in literature of Froude <5 matches well to the gravitational settling regime observed in the transparent airway. For Froude >5 mainly the inertial impaction is observed as mechanism for aerosol deposition in this set-up. An error analysis is performed for evaluating the influence of the low relative humidity of the inhaled air on the aerosol evaporation and deposition. This feasibility study shows the capability of the measurement method in combination with the airway model to resolve the aerosol deposition up to the eighth bifurcation. In future, this analysis should be extended to higher airway generations by microscopic LIF imaging to evaluate the deposition mechanisms in all 23 generations of the transparent airway model.

* Corresponding author.
E-mail address: guerzing@wsa.rwth-aachen.de (S. Gürzing).

https://doi.org/10.1016/j.jaerosci.2025.106634
Received 8 February 2025; Received in revised form 3 June 2025; Accepted 10 June 2025
Available online 16 June 2025

1. Introduction

1.1. Main influencing parameters for aerosol deposition mechanisms in the human lung

Delivering therapeutics to targeted regions in the lungs is a major challenge (Borghardt et al., 2018). Effective drug administration is crucial for managing a range of lung diseases, including asthma, acute respiratory distress syndrome (ARDS) or chronic obstructive pulmonary disease (COPD) (Artigas et al., 2017; Barjaktarevic & Milstone, 2020; McCracken et al., 2017). Modern treatments rely mainly on delivering medication through nebulizer- and inhaler-generated aerosols or powders, which are inhaled either by mechanical ventilation or by spontaneous respiration. The site of drug delivery in the human lung with the aim of distal airway penetration and a uniform drug distribution is important for the efficacy of the delivered drug and is mainly dependent on i) the aerosol size containing the drug, on ii) the respiration, and on iii) the type of inhalation device (Borghardt et al., 2018). Other parameters are the patient-specific variability of the lung anatomy, which influences the local respiratory flow behavior, and the disease-specific inhalation profile of the patient (Williams et al., 2022, 2024).

Nebulizers deliver the drug-containing aerosol in a continuous mode whereas soft mist inhaler, dry-powder inhaler and pressurized metered-dose inhaler need to be actuated by the patient's inspiratory flow or manually by device actuation which requires a proper handling of the device (Barjaktarevic & Milstone, 2020). Depending on the device different breathing patterns are required for a correct and effective delivery of drugs (Barjaktarevic & Milstone, 2020). The size of aerosols in combination with the respiratory flow rate determine the deposition field in the human lung. Large particles (>5 μm) tend to deposit in the mouth and the upper airways, whereas smaller particles (0.5–5 μm) are delivered more distally into the lungs, partially reaching the alveolar region (Borghardt et al., 2018; Sznitman, 2013). The deposition mechanisms such as i) the inertial impaction, ii) the gravitational settling or sedimentation, and iii) the Brownian diffusion influence the site of pulmonary drug delivery and are highly dependent on the aerodynamic diameter of the drug-containing aerosol or particle (Carvalho et al., 2011).

The inertial impaction is related to the incapability of the aerosol to follow the inhaled air stream due to the inertial momentum of the aerosol. During directional changes of the air stream as for example in bifurcations, the inertia of the aerosol leads to differing trajectories to the air stream resulting in collisions with the airway walls (Carvalho et al., 2011; Darquenne, 2012). The probability of inertial impaction is estimated by the non-dimensional Stokes number. The Stokes number is calculated as

$$St_i = \left(\rho_p \, d_p^2 \, U_i\right) \; / \; (18 \, \mu \, D_i) \tag{1}$$

with d_p as particle diameter and ρ_p as particle density. U_i is the average air velocity, D_i is the diameter of the airway generation i and μ is the dynamic viscosity of air. The Stokes number represents the ratio of the particle response time to the characteristic flow time scale (Tropea et al., 2007). Large Stokes numbers refer to inertial impaction, whereas low Stokes numbers refer to a stream-following aerosol whose deposition behavior is affected by gravitational settling or Brownian diffusion. According to Sznitman et al. (Sznitman, 2013) aerosols with $d_p > 8$ μm tend to deposit by inertial impaction whereas for aerosols in the range $1 < d_p < 8$ μm the deposition mechanism of gravitational settling is prevalent. Inertial impaction is mostly important in the extra-thoracic and the upper airways due to high flow velocities and are mostly found in the bifurcations on the carinal ridge (Comer et al., 2001; Zeng et al., 2000).

For estimating the influence of gravitational settling, a sedimentation parameter γ_i is proposed in literature (Chen et al., 2018; Kleinstreuer et al., 2007):

$$\gamma_i = \left(v_{settling} \, L \cos \theta_i\right) / \left(U_i \, D_i\right) \tag{2}$$

with the airway tube length L, the airway inclination angle θ_i to the horizontal and the settling velocity $v_{settling}$, defined as

$$v_{settling} = \left(\rho_p \, g \, d_p^2\right) \; / \; (18 \, \mu) \tag{3}$$

with g as gravitational acceleration. Gravitational settling dominates for $\gamma_i > 0.1$ and inertial impaction dominates for $\gamma_i < 0.001$ according to Kleinstreuer et al. (Kleinstreuer et al., 2007). Note that the proposed sedimentation parameter is evaluated for aerosol diameter between 1 and 10 μm. However, for very small particles below that range the sedimentation parameter could lead to values below 0.001 indicating the deposition mechanism of inertial impaction. For very small particle sizes the inertial impaction is negligible due to very low Stokes numbers and the ability to follow the air stream.

The dominance of gravitational settling is time-dependent (Zeng et al., 2000); Certain breathing behaviors such as breath-holding improve drug deposition by this deposition mechanism due to a longer duration of zero air velocities in the airways (Zeng et al., 2000). Aerosol deposition due to gravity occurs more likely in the lower bronchial and alveolar regions where respiratory flow rates are low (Zeng et al., 2000).

The diffusion by Brownian motion is dominant for aerosols smaller than 0.5 μm in diameter (Sznitman, 2013) and is inversely dependent on the aerosol diameter as shown in the following formula (Carvalho et al., 2011; Darquenne, 2012)

$$D_B = (k \, T) \; / \; \left(3 \, \pi \, \mu \, d_p\right) \tag{3}$$

with the diffusion coefficient D_B, the Boltzmann's constant k, and the absolute temperature T. Especially nanosized particles (<200 nm) are depositing in all regions of the lung by Brownian diffusion (Cheng, 2014). However, this deposition mechanism is dominant in the alveolar region, due to the low air velocities in this region with immediate proximity to the alveolar walls and because this region is mainly reached by aerosols below 2 μm in size (Darquenne, 2012; Sznitman, 2013; Xi et al., 2020; Zeng et al., 2000).

For the development of adequate inhalation therapies, the three parameters aerosol size, inhalation device, and respiratory flow need to be optimized with respect to the resulting deposition fields due to the interplay of the different deposition mechanisms throughout the breathing cycle. Therefore, deposition field visualization and analysis are needed for the evaluation of the effectiveness of inhalation therapies.

1.2. Aerosol deposition analysis by in-vivo imaging techniques

In-vivo imaging techniques of aerosol deposition fields in the human lung are currently performed by the inhalation of radio-labelled tracers. Nuclear imaging techniques such as 2D-scintigraphy, Single Photon Emission Computed Tomography (SPECT) or Positron Emission Tomography (PET) (Conway, 2012; Lizal et al., 2018) deliver more qualitative information on the total and regional lung deposition fields in the human lung than a quantitative evaluation of the accurate aerosol deposition location. These techniques are lacking certain detection accuracies on the deposition fields due to the low spatial image resolution, low temporal resolution, disturbing motion effects of the breathing subject, and, in the case of 2D-scintigraphy, the projection of the deposition field onto a 2D image (Lizal et al., 2018). The lacking spatial resolution leads to indistinguishable airways, particularly after the upper airways. Consequently, the aerosol deposition cannot directly be allocated to certain airway generations (Conway, 2012). The quantification of aerosol deposition with 2D-scintigraphy imaging leads to varying results due to the arbitrary segmentation of the 2D image into different region of interests, i.e. the non-standardized definition of central and peripheral lung regions, in various laboratories (Biddiscombe et al., 2011). The more complex imaging technique SPECT combined with computer-tomography (SPECT-CT) leads to improved aerosol deposition analysis in comparison to 2D imaging. The measured 3D data of deposited aerosols can be divided into ten three-dimensional 'shells', with the first shell representing the central region around the hilum and the tenth shell representing the most peripheral region of the lung (Conway, 2012; Dugernier et al., 2017). Despite the more physiological data segmentation it remains an arbitrary approach with the need of standardization (Conway, 2012; Dugernier et al., 2017). However, the arbitrarily segmented shells can be correlated to airway generations by using the theory of Weibel's model (Fleming et al., 2004).

Overall, the current in-vivo imaging methods are restricted to the total and regional pulmonary deposition in a broad manner, divided in central and peripheral regions or shells (Dugernier et al., 2017). The distribution of aerosol deposition is not evaluated at the local level of individual airway generations or at sub-airway resolution, and consequently, no conclusions can be drawn about the actual site of drug action, which may be important for estimating the efficacy of inhalation therapy.

1.3. Aerosol deposition analysis by in-vitro measurement techniques

Current research on more detailed aerosol deposition fields in the human lungs involves mainly numerical simulations (*in-silico*) to enable a better understanding of the transport mechanisms and their resulting deposition patterns (Feng et al., 2021; Hofmann, 2020; Islam et al., 2020). In comparison, experimental in-vitro research on aerosol deposition in a holistic human lung replication is lacking due to the complexity of replicating the human lung from the extra-thoracic airways starting with the mouth or nasal cavity over the upper airways to the alveoli. The airway diameter varies from the trachea to the alveoli with a factor of 45 with a simultaneous change of the volume flow rates by a factor of 10^7 (largest to smallest volume flow rate) (Möller et al., 2021; Yeh & Schum, 1980). The technical realization of a holistic human lung replication requires a high manufacturing accuracy for the complex lung geometry and demands a sophisticated technical system for controlling the flow rates over several airway generations. Further, the number of airways increases exponentially with every generation which increases further the complexity of the replication system (Ahookhosh et al., 2020).

Several *in-vitro* studies examined the flow structure in the upper human airways (Groβe et al., 2007; Janke et al., 2019; Xu et al., 2020) and in the acinar region (Berg et al., 2010; Oakes et al., 2010; Sera et al., 2021) by Particle Image Velocimetry (PIV). Few experimental in-vitro studies of the human lung exist regarding i) the liquid aerosol deposition (Cheng et al., 1999; Holbrook & Longest, 2013; Nordlund et al., 2017; Su & Cheng, 2009; Zhang & Finlay, 2005; Zhou & Cheng, 2005), ii) the dry particle deposition (R. Delvadia et al., 2013; R. R. Delvadia et al., 2012; Holbrook & Longest, 2013) and iii) the fiber deposition (Su & Cheng, 2006a, 2006b, 2009).

The *in-vitro* studies for i) the liquid aerosol deposition and iii) the fiber deposition focus mainly on the upper airways considering all branches and the mouth-throat geometry, are based on steady flow rates and measure *ex-situ* the integral mass of aerosol deposition in segmented lung model areas after a certain measurement time. In Zhang et al. (Zhang & Finlay, 2005) aerosol deposition is measured in a fully reconstructed, idealized and planar lung model from the mouth to the third generation by gravimetry of segmented parts and filters at the outlets of the lung model. A similar approach of measuring deposited aerosols at filter positions and segmented model parts is used by Zhou et al. (Zhou & Cheng, 2005) and Cheng et al. (Cheng et al., 1999) by the method of fluorescence spectrometry to determine the mass of aerosol deposition. The lung model in both cases is fully reconstructed up to the third generation by using a lung cast of a human cadaver. By coating the same lung model by silicon oil, the lung model was able to capture fibers such as carbon, glass or TiO_2 fibers at the deposited position. The fractional deposition was calculated by washing out the segments and counting the fibers under the microscope (Su & Cheng, 2006a, 2006b, 2009). Nordlund et al. (Nordlund et al., 2017) extended the fully reconstructed human lung model based on casts to the seventh generation and measured the content of deposited aerosols in each segment by gas chromatography-mass spectrometry.

For the deposition analysis of ii) dry particles, a lung model with idealized geometry and asymmetric bifurcations up to the third generation was used for testing dry particle inhaler (DPI) (Delvadia et al., 2013; R. R. Delvadia et al., 2012). Similar to the in-vitro approach for fiber deposition the lung model was coated in order to create a wet surface for capturing the dry particles. A breath

simulator created a global transient inhalation profile for the application of the different inhaler devices. The drug deposition in the coarse segments of the mouth-throat, the trachea-bronchi, the plexiglas housing and a filter were analyzed by high-performance liquid chromatography. A higher spatial resolution was achieved by Holbrook et al. (Holbrook & Longest, 2013) in the planar and asymmetric generations 3 to 5 by the use of fluorescent particles with steady flow rates. Here, the particles were counted via a microscope in 0.75 mm squares in each disassembled half of the model leading to a grid showing the locally resolved deposition fraction.

These in-vitro studies show the potential of experimental research on liquid aerosol, particles or fiber deposition and were partially able to increase the spatial resolution to distinct airway generations and bifurcations in comparison to in-vivo studies. The calculation of regional deposition fractions (Nordlund et al., 2017), deposition efficiencies (Cheng et al., 1999; Nordlund et al., 2017; Zhang & Finlay, 2005; Zhou & Cheng, 2005) and IVIVICs (Longest & Holbrook, 2012a, 2012b) lead to the possibility of validating theoretical models (Zhou & Cheng, 2005) or numerical simulations (Nordlund et al., 2017) and to the correlation of in-vivo with in-vitro measurements (Longest & Holbrook, 2012a, 2012b). Due to the restriction on mostly constant flow rates (15–90 L/min) and the limitation of representing the upper lung geometries, the deposition mechanism of inertial impaction is overrepresented. The influence of gravitational settling is reduced by the lack of low flow rates which are apparent in physiological breathing cycles. The deposition analysis is spatially limited to segments of the lung model and due to the ex-situ measurement method, the temporal resolution of the deposition analysis is lacking.

1.4. Aerosol deposition analysis by optical in-vitro measurements in the transparent airway model

In contrast to the *in-vitro* models found in literature, the idealized airway model in this study does not consider all branches up to a certain airway generation, but replicates a representative respiratory tract of the left lower lobe from the trachea to the 23rd generation (Gürzing et al., 2022; Möller et al., 2021). An extra-thoracic airway is implemented on top of the trachea. The airway has a planar configuration with symmetrical bifurcations. These simplifications lead to the possibility to optically capture the whole airway model in one camera view leading to a simplified camera set-up and fast measurements. Instead of constant flow rates, a more physiological respiratory cycle with inhalation and exhalation is realized. The airway model is manufactured in fused quartz glass with polished surfaces which ensures a high surface quality. The transparency and surface quality of the model allow the use of optical measurement techniques, with the possibility of microscopic imaging down to the smallest airways. In former studies, optical measurement methods such as high-speed shadowgraphy or laser-induced fluorescence (LIF) are used to visualize aerosols streaming in the air (Möller et al., 2021) or the deposition and behavior of large liquid plugs and films in the airway model (Gürzing et al., 2022). By using optical *in-situ* measurement techniques such as laser-induced fluorescence, no physical segmentation of the airway model is required for the investigation on aerosol deposition. This leads to the possibility to visualize aerosol deposition in real-time with a higher temporal and spatial resolution i.e. on the level of airway generations and even sub-airway resolution in comparison to the segmented in-vitro models in literature (compare to section 1.3). With these technical advantages the airway model may improve the fundamental understanding of aerosol deposition mechanisms by experimental in-flight (Möller et al., 2021) and deposition field measurements (Gürzing et al., 2022). Secondly, the airway model can be used to rapidly test the deposition fields of different inhalation devices and, thirdly, the airway model can serve as a validation tool for numerical simulations and theoretical models in future. However, the geometrical simplifications in the airway model as the idealized airway geometry, symmetrical bifurcations, a planar configuration, and the restriction to the left lower lobe needs to be validated against *in-vivo* studies in terms of flow structure and aerosol deposition.

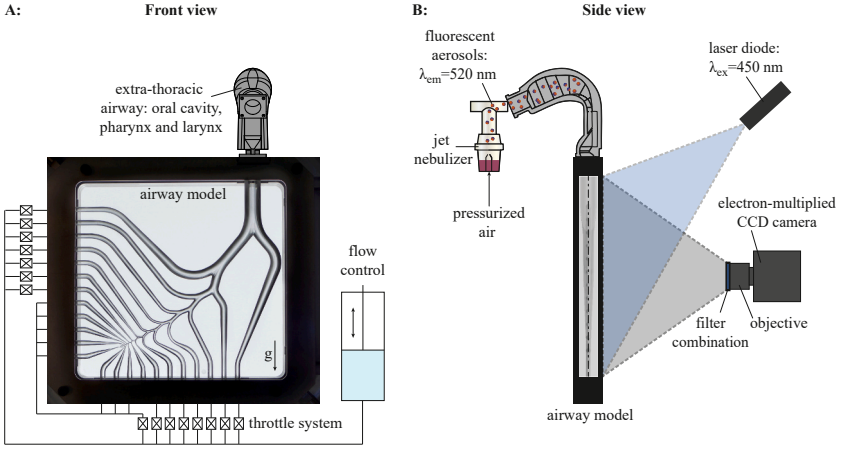

Fig. 1. Concept of the test rig and the measurement method of laser-induced fluorescence (LIF). A: Transparent airway model in front view with mounted extra-thoracic airway (ETA) and connected piston pump with throttling system to control breathing cycle and volume flows in each airway generation. B: LIF measurement method, which consists of a CW laser diode (emitting an expanded laser beam on the transparent airway model to excite the fluorescent dye in the aerosols) and an EMCCD camera with objective and filter combination (imaging the fluorescence of the deposited aerosols). The fluorescent aerosols are produced by a jet nebulizer.

In this study, the general feasibility of the transparent airway model for an *in-situ* LIF analysis of the aerosol deposition is assessed. The aerosol deposition from the 1st to the 10th bifurcation is evaluated regarding the involved deposition mechanisms and is compared with the existing literature using relevant dimensionless numbers. The influence of the inhaled air humidity on the physiological interpretation of aerosol deposition in a currently non-self-humidifying airway model is also evaluated.

2. Material and methods

2.1. Composition of the airway model and respiratory cycle

The transparent airway model shown in Fig. 1A and more detailed in Fig. 3A combines two different lung models from literature, the "typical Path Lung Model" of the left lower lobe by Yeh and Schum (Yeh & Schum, 1980) and the "Physiologically Realistic Bifurcation Model" (PRB) by Heistracher and Hoffmann (Heistracher & Hofmann, 1995). More information on the airway geometry is summarized in Möller et al. (Möller et al., 2021). The airway model comprises one representative pathway of a male left lower lobe from the trachea (generation 0, abbreviated as G0) to the highest airway of the human lung (G23). Its geometry is aligned in a planar way, meaning there is no rotation of the bifurcations out of the plane. This planar arrangement provides optical access to the entire airway model and allows to evaluate all generations simultaneously by a single camera shot, ensuring optimal comparisons between different locations. The airway model is mounted in such a way that the symmetry plane and the trachea are vertically aligned, i.e. in direction of gravity, as shown in Fig. 1. Note that the chosen orientation has a great impact on the gravitational settling of the aerosols. An idealized extra-thoracic airway (ETA) is implemented as 3D-print to the inlet of the airway model for a more physiological inflow. This geometry is based on existing literature ("Alberta model") and consists of the oral cavity, pharynx, epiglottis, and larynx with the exclusion of nasal features (Azarnoosh et al., 2020; Heenan et al., 2003; Johnstone et al., 2004). As indicated in Fig. 1B, a standard medical jet nebulizer (item nr. 30148, Hsiner CO., LTD, Taiwan) is placed in front of the ETA, with the horizontal exit channel as close as possible to the angled inlet of the ETA. The jet nebulizer generates a fine mist of aerosols with pressurized air of 1 bar (gauge). The inlet of the jet nebulizer's flow channel (on the left) is closed for guiding the outflowing aerosols into the direction of the airway model (to the right). The small gap between the exit channel of the jet nebulizer and the ETA allows ambient air to enter the airway model during inhalation. Using the phase Doppler technique, the aerosol mist at the outlet of the jet nebulizer is characterized with an arithmetic mean diameter D_{10} of 4.43 µm and a Sauter mean diameter D_{32} of 14.58 µm by Möller et al. (Möller et al., 2021). Further, the mass median aerodynamic diameter MMAD is 24.44 µm and the geometric standard deviation GSD is 1.64, indicating a polydisperse aerosol distribution.

The breathing pattern in the airway model is generated via a piston pump which is controlled by a stepper motor (drylin® ZLW-1040, igus GmbH, Germany) and an in-house control software (LabVIEW, National Instruments Corp., USA). As described in Möller et al. (Möller et al., 2021) an overall breathing pattern with a tidal volume of 0.5 L (based on 7 mL/kg bodyweight) and maximum flow rate of 0.5 L/s (Kleinstreuer et al., 2007) is chosen to simulate the breathing at rest of a healthy person with a bodyweight of 70 kg (Larsen, 2016; Westhoff & Rühle, 2011). The implemented flow-volume curve of the breathing pattern is shown in Fig. 2B. The physiological values of the chosen tidal volume and maximum flow rate of 0.5 L/s are combined in a sinusoidal flow-volume curve for the inspiration and expiration. This shape leads to the respiratory flow rate over time as shown in Fig. 4A.

The volume flow of the piston pump is distributed to the generations by a throttle-rotameter-system (Omega Engineering, Inc., USA) (Möller et al., 2021).The volume flows from G1 to G14 are separately adjusted, while one single rotameter-throttle-system controls the flow rate from G15 to G23 due to the low flow rates in these generations. A physiological asymmetric flow distribution is set at the lobar bronchi with 46 % of the total volume flow for G1 in the respiratory tract (left lobe of the lung) and 31 % at G2 (left lower lobe) in accordance to Longest et al. (Longest et al., 2012). In subsequent bifurcations the flow division is assumed to be symmetric (Longest et al., 2012; Möller et al., 2021).The room temperature during measurements is constant at 21 °C, and the air

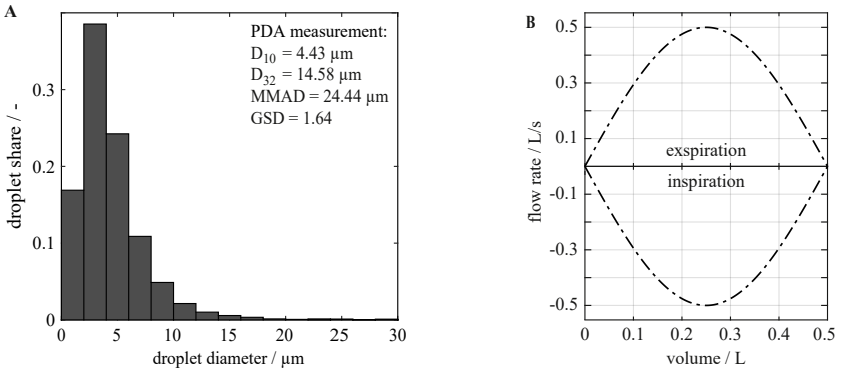

Fig. 2. A: Measured droplet size distribution of the used jet nebulizer (Möller et al., 2021). B: Implemented flow-volume curve for tidal breathing, calculated with the specific breathing volume of 7 mL/kg for a person of around 70 kg weight (Larsen, 2016; Westhoff & Rühle, 2011) and a maximum flow rate of 0.5 L/s (Kleinstreuer et al., 2007).

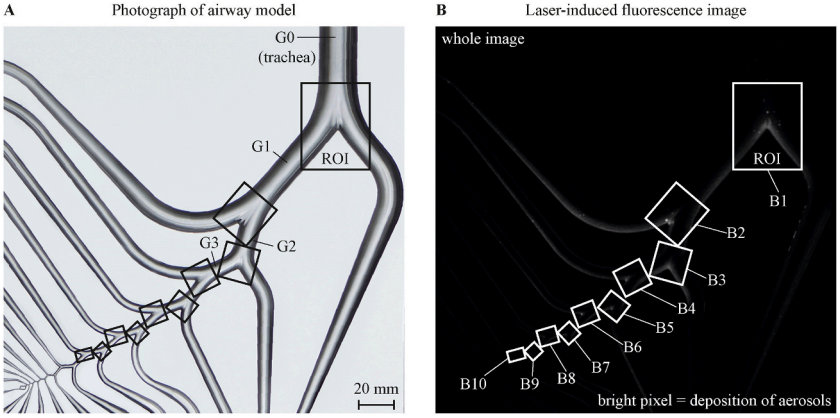

Fig. 3. A: Photograph of the airway model with indication of the generations G0 to G3 and regions of Interest (ROI) representing the bifurcations. B: Averaged LIF image by laser-induced fluorescence at time step t = 5.8 s. White boxes define the ROIs of bifurcations B1 - B10 for image post-processing. Bright pixel represents an accumulation of deposited aerosols.

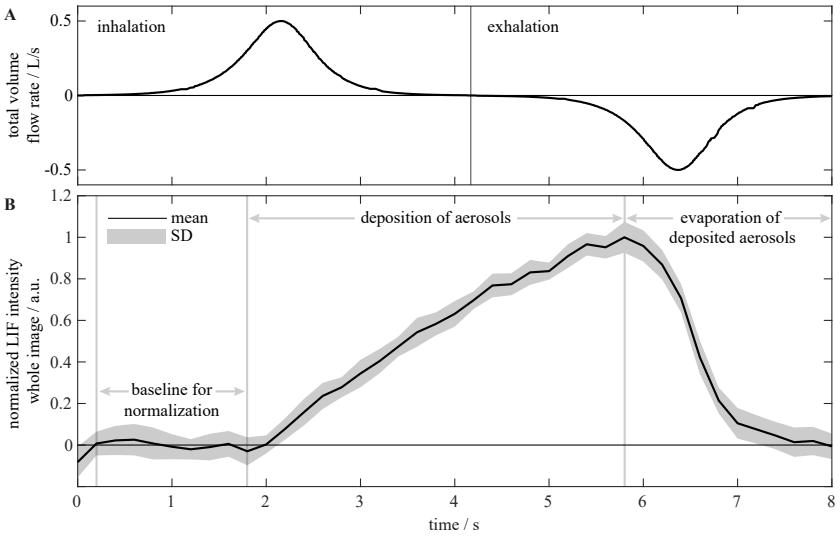

Fig. 4. A: Breathing cycle, shown as total volume flow (L/s) over time (s). B: Normalized LIF intensity of the whole image over time, averaged over ten breathing cycles. The increase of signal is attributed to the deposition of aerosols, whereas the decrease of signal can be assigned to the evaporation of deposited aerosols.

humidity is estimated to be in the range of 40 %–60 % relative humidity (RH).

2.2. Visualization of aerosol deposition by laser-induced fluorescence

For the purpose of visualization of deposited aerosols in the airway model, the laser-induced fluorescence (LIF) technique is used. A soluble fluorescent tracer pyranine (item number: H1529-1G, Merck, Germany) is added to deionized water (0.05 % w/v). This solution is embedded into the jet nebulizer for producing fluorescent aerosols. Further, the beam of a CW laser diode (60 mW, Picotronic GmbH, Germany) with a wavelength of 450 nm is expanded in order to fully illuminate the airway model. The fluorescent dye in the deposited aerosols is excited by the laser diode and emits fluorescence light with a central wavelength of approximately 520 nm. This fluorescent light is captured by an electron-multiplying CCD camera (iXon$_3$ 888, Andor Technology Ltd., Northern Ireland) with an objective lens (50 mm, 1:1.2, NIKKOR, Nikon, Japan), resulting in a scale of 0.22 mm/pixel. A filter combination in front of the lens consisting of a bandpass filter (CW: 515 nm ± 10 nm, Thorlabs, Inc., USA) and a long-pass filter (cut-on wavelength: 475 nm, Qioptiq Linos Inc., USA) filters out reflected laser light. The camera is synchronized and triggered to the start of each inhalation, capturing each breathing cycle with 41 images at a rate of 5 fps with an exposure time of 0.05 s. In total, the LIF signal of depositing aerosols in the airway model is imaged over ten subsequent breathing cycles with a total measuring time of 83.06 s. The resulting LIF images are represented in 16-bit grayscale images.

2.3. Post-processing of laser-induced fluorescence images

The LIF images are evaluated in ten different regions of interest (ROIs) as shown in Fig. 3B, each representing the respective bifurcations B1 to B10 consisting of airway generations G0-G10. The locally resolved LIF intensity within the ROIs can be used as an indicator for the deposition performance in the bifurcation; the LIF intensity in each pixel is expected to correlate with the mass of deposited aerosols.

For further discussion on deposition performance, the LIF images are post-processed as follows over the whole image and within the ROIs.

1) The LIF images of the ten sequential breathing cycles are used to generate an averaged set of LIF images over the breathing cycle. The arithmetic averaging is performed for each measured time point within the breathing cycle (41 images at a rate of 5 fps, triggered to the start of each inspiration).
2) For eliminating the remaining laser light on the LIF images, a background subtraction is applied leading to a better visualization of the aerosol deposition. The first averaged LIF image at time point t = 0 s (start of the inspiration) is taken as reference image for reflected laser light and is subtracted from all averaged LIF images. Note that this first image does not include fluorescent signal.
3) In each ROI and the entire image, a mean LIF intensity value (hereafter referred to as "LIF intensity") is calculated over the chosen area, for each time step in the breathing cycle. Due to the previous subtraction of the reference image of the laser light (corresponding to the first averaged LIF image), the LIF value of the first time step (t = 0 s) is exactly zero. Because of the signal noise in the camera chip, the LIF values of the subsequent time steps are slightly elevated compared to the first image, although no aerosol deposition is visible.

4) For a better comparability between the ROIs, a normalization is performed on the LIF intensities of each ROI between the baseline intensity and the maximum intensity, resulting in the LIF intensity curves shown in Figs. 4B and 5C. The baseline intensity is the average intensity between t = 0.2 s–1.8 s. In this timespan, no aerosol deposition is detected in the LIF images and in the mean LIF intensities in Figs. 4B and 5C. This is plausible if the arrival time of the first aerosols to the location of B1 is considered. A conservative estimation on the arrival time of the first aerosols to B1 is calculated to 1.84 s, based on the actual volume flow rate as well as the lengths and diameters of G0 (L = 100 mm, D_i = 20.1 mm) and of the extra-thoracic airways (L = 235 mm, D_i = 20.1 mm). The ETA consists of a complex geometry and one of the smallest diameters of the ETA (D_i = 20.1 mm) is taken as calculation basis for the conservative estimation, resulting in a faster estimated arrival time of the aerosols. Therefore, slightly longer arrival times are expected in the airway model.
5) The LIF gradient in Fig. 5D is calculated by the forward difference of the normalized LIF intensities from Fig. 5C. Through the forward difference calculation, the LIF gradient appears slightly shifted to the left in comparison to the measured LIF intensities.

For a better understanding of the post-processing of the data, the videos showing i) the measured LIF images over ten breathing cycles, ii) the averaged LIF images, and subsequently iii) the LIF images (averaged and unaveraged) with subtracted laser reference are provided in the supplementary data. Furthermore, the standard deviations (SD) of the mean LIF intensity of all ROIs and the laser reference image are shown in the supplementary data.

3. Results and discussion

3.1. Deposition and evaporation of aerosols in the whole airway model

The total volume flow rate of the respiratory cycle is plotted over time in Fig. 4A. In comparison, the normalized LIF intensity of the whole image is shown in Fig. 4B. In the following, characteristics of the intensity curve will be described and related to transport mechanism at droplet level.

The LIF intensity progression over the breathing cycle in Fig. 4B can be subdivided in three different time-intervals, each showing a characteristic behavior: i) a time-interval with low and stagnant LIF intensity, containing the minimum baseline for normalization (t = 0.2–1.8 s), ii) a time-interval with nearly continuous increase of the LIF intensity (t = 1.8–5.8 s) and iii) a time-interval with decreasing LIF intensity until reaching the baseline again (t = 5.8–8 s).

In the first time-interval no aerosol deposition is seen in the airway model. As estimated in a conservative calculation in section 2.3. The first inhaled aerosols arrive at the first bifurcation B1 after t = 1.84 s and thereafter at subsequent bifurcations. Note that due to the post-processing (subtraction of the laser light reference in step 2) no LIF signal is apparent in the first LIF image. This LIF value is shifted into the negative through the normalization between the baseline and maximum LIF value.

In the second time-interval between t = 1.8 s–5.8 s a rising fluorescence is captured by the optical system, indicating aerosol deposition in the airway model. The deposition starts approximately at the inflection point of the inhalation flow rate and ends similarly around the inflection point of the exhalation flow rate. When the inhalation flow rate decreases close to 0 L/s at t = 3.5 s, the normalized LIF intensity in Fig. 4B is around 0.5, indicating that only half of all deposited aerosols have been impacted during inhalation at higher flow rates. The other half deposits afterwards during low flow rates and even at slightly elevated flow rates during exhalation. Note that the above results are based on an integral evaluation of the entire image and thus include not only the entire representative airway tract but also non-physiological geometries such as the exit channels of the individual airway generations. However, this LIF intensity behavior of the whole image shows that both - low as also higher flow rates - are contributing to the

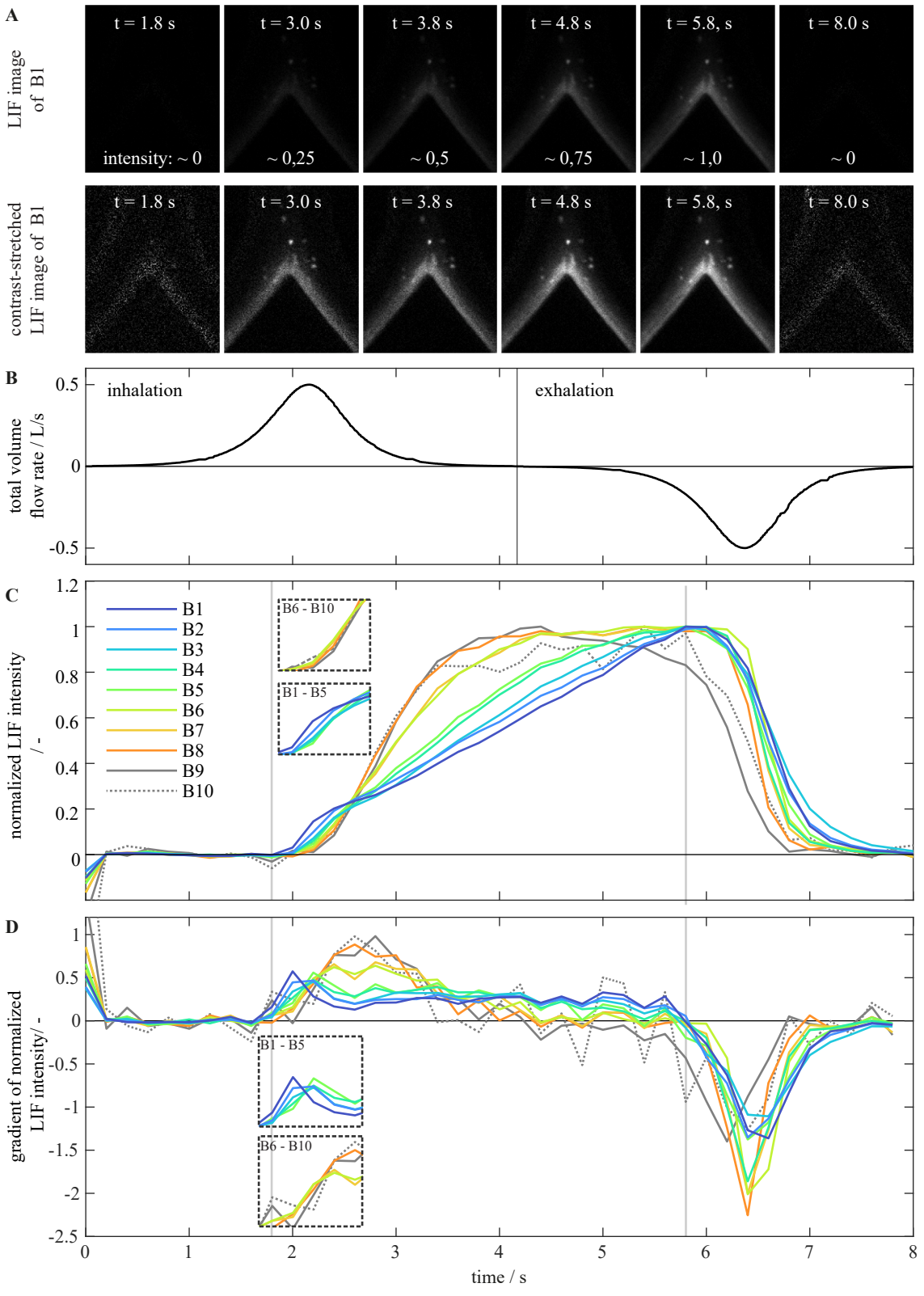

(caption on next page)

Fig. 5. A: LIF images and contrast-stretched LIF images of B1 at different time points in the respiratory cycle. B: Breathing cycle, shown as total volume flow (L/s) over time (s). C: Normalized LIF intensity for 10 bifurcations over time, averaged over ten breathing cycles. Standard deviations are summarized in Table 1 and are shown in more detail in the supplementary data. D: Gradient of normalized bifurcation intensity calculated by using forward differences. The dashed boxes allow a more detailed visualization of the LIF intensity curves in dense areas of the plot.

deposition of aerosols. This implies the influence of different aerosol deposition mechanisms such as inertial impaction during higher flow rates and gravitational settling during low flow rates. A more detailed analysis of the responsible transport mechanisms will be performed in the evaluation of the LIF intensities of the bifurcations without remaining unphysiological geometries in the next section 3.2.

The third time-interval shows the decrease of LIF intensity to the initial LIF baseline starting with increasingly higher exhalation flows. This behavior is explained by the evaporation of the deposited aerosols in the airway model. After evaporation the tracer loses its fluorescence in dry state and cannot be captured by the camera set-up. During exhalation, air with low relative humidity originating from the piston pump and the tubes to the airway model streams over the deposited aerosols, causing evaporation of the deposited droplets through convection. The inhaled and exhaled air stream in the airway model is not regulated to physiological values of nearly saturated air with 99.5 % RH and 37 °C air temperature downstream the trachea (Ferron et al., 1988) and fast evaporation can take place at room temperature of 21 °C and a moderate estimated room humidity in the range of 40–60 % RH. For reference, a water droplet with a 10 µm diameter completely evaporates in 0.2 s in stagnant air at 20 °C and 50 % RH, whereas the droplet lifetime increases to around 13 s at physiological conditions of 37 °C and 99.5 % RH (G. Ferron & Soderholm, 1990). Therefore, the influence of unregulated air humidity in the airway model and of the inhaled air on the physiological relevance of the deposition measurements is closely assessed in section 3.5.1.

3.2. *Aerosol deposition over bifurcations B1 to B10*

In this section a bifurcation-specific discussion on the deposition behavior is carried out, based on the normalized LIF intensity and its temporal gradient. Fig. 5A shows an exemplary sequence of the recorded and contrast-stretched LIF images of bifurcation B1 over the respiratory cycle. Contrast-stretching is a method for increasing the contrast in the image. The minimum and maximum available grey value is adjusted to the entire value range of a 16-bit image. The contrast-stretched LIF images are shown for a better visualization of the deposition pattern.

The LIF images and contrast-stretched LIF images of B1 show qualitatively the temporal course of aerosol deposition over the breathing cycle, based on the quantitative change of LIF intensity in Fig. 5C. The LIF images show a gradual increase in LIF intensity and thus aerosol deposition at the bifurcation. The bifurcation is brightest at t = 5.8 s with a maximum normalized LIF intensity of 1. The brightness in the LIF image is highest at the carinal ridge (center of the image) and gradually decreases on the inner sides of the bifurcation into distal direction. A high aerosol deposition at the carinal ridge is typical for the deposition mechanism of inertial impaction (Nicolaou, 2018; Ou et al., 2020). However, the aerosol deposition may also be influenced by gravitational settling since the inner sides of the bifurcation are in the direction of gravity. Therefore, a quantitative evaluation of the deposition as shown in Fig. 5C is necessary in order to analyze the deposition mechanisms in more detail. The individual bright spots in the LIF images are irregularities in the airway model where the light of the fluorescent aerosols refracts towards the camera.

In Fig. 5C, for all bifurcations investigated (B1 – B10), the overall behavior of normalized LIF intensity (as indicator for deposition behavior) shows a similar trend as the previously introduced normalized intensity of the whole image (comp. to Fig. 4B): Low LIF intensities are observed in the baseline time-interval between t = 0.2–1.8 s. In the second time-interval at t = 1.8–5.8 s the LIF intensities are increasing and reaching a maximum at t = 5.8 s for all bifurcations except for B9 which reaches the maximum earlier at t = 4.4 s. The rate of intensity increase differs for each bifurcation and will be discussed below in detail. After reaching the maximum the LIF intensity of all bifurcations decreases back to the baseline in the third time-interval at t = 5.8–8 s. During signal decrease the progressions of LIF intensities of B1 - B8 are similarly aligned whereas B9 and B10 show an earlier and faster signal loss.

The LIF intensity curves of B9 and B10 show stronger fluctuations over time in comparison to the other bifurcations. This can be explained by a reduced signal-to-noise ratio, resulting from the small size of both ROIs (ROI pixel number <1000, see Table 1) combined with the exponential decrease in flow rate over bifurcations, resulting in fewer aerosols reaching these bifurcations. This is also represented in the increased standard deviations (averaged over the time of the breathing cycle) for B9 and B10 with 0.086 and 0.122 than the other bifurcations (<0.06) and the whole image (<0,062) as stated in Table 1. Therefore, B9 and B10 are excluded in the remaining analysis of this study. It is expected that deeper airway generations and bifurcations could be investigated in future, if spatial resolution as well as the fluorescence intensity of the tracer will be increased.

In the second time-interval, the increase of LIF intensity varies between each bifurcation. As shown in Fig. 5C, the onset of LIF intensity increase can be firstly observed for B1 and is followed up by the subsequent bifurcations. Further, a switch from left to right curved behavior is seen for the intensity profiles B1 to B5 whereas a left curved intensity profile is recognized for B6 to B8 (comp. dashed boxes in Fig. 5C) around t = 1.8–2.8 s. These curve progressions at the start of aerosol deposition are accompanied with higher inhalation flows. This is followed up by a linear increase at different rates for each bifurcation at lower respiratory flow rates, with the highest slope for B8 and the lowest slope for B1. The maximum intensity is achieved by a transition from the linear increase to a flat curve at different times for each bifurcation. B8 approaches its intensity maximum around t = 4 s and B1 at t = 5.8 s, the other bifurcation intensity curves lie in between.

Fig. 5D shows the gradient of the normalized LIF intensity and is a measure for the aerosol deposition rate per time step whereas the

Table 1
Standard deviations (SD) of the normalized LIF intensities of each ROI, averaged over the time of the breathing cycle.

ROI	Whole image	B1	B2	B3	B4	B4	B6	B7	B8	B9	B10
SD	0.062	0.025	0.030	0.030	0.034	0.041	0.047	0.058	0.060	0.086	0.122
Pixel number	1.048.576	31800	10827	6692	4428	2717	2417	1461	1608	981	952

LIF intensity in Fig. 5C correlates to the accumulated deposited aerosols to this time step. After t = 1.8 s the first aerosols deposit in the bifurcations during higher respiratory flow rates as seen in Fig. 5C. This is reproduced in the LIF gradient curves showing distinct maxima or peaks for B1 to B5, which are indicators of the inflection points from the left to right curved behavior in Fig. 5C. The higher the bifurcation number the more the maxima are temporally shifted to later time steps. After reaching the maxima from B1 to B5, the LIF gradient immediately decreases (resulting in a visual peak in the LIF gradient) and transitions to a constant gradient for low to zero inhalation flow rates. By comparison, the gradient maxima of B6 to B8 are reached at later time steps and are immediately followed up by constant values around the maximum value without the intermediate step of decreasing gradients. The duration of the constant gradients varies between the bifurcations. For B1 the constant gradient endures until the evaporation during exhalation starts (t = 5.8 s), whereas for B8 the constant gradient is apparent until t = 3 s and deceases to zero afterwards. All other bifurcations show a gradual transition between the LIF gradient curves of B1 and B8. The constant gradient in Fig. 5D represents the linear increase in LIF intensity in Fig. 5C and the subsequent decrease of the LIF gradient to zero corresponds to the convergence of the LIF intensity to the maximum in Fig. 5C.

These described differences in the intensity curve behaviors from B1 to B8 indicate varying predominant aerosol deposition mechanisms in the human lung at certain time points of inhalation: high breathing flow rates at the beginning of aerosol deposition promote inertial impaction of aerosols which is expected to be the dominant deposition mechanism in the upper lung geometry. This is confirmed by the observed maxima of B1 to B5 which are represented by a rising and instantly decreasing gradient behavior at higher flow rates. It is expected that the aerosol deposition caused by inertial impaction correlates linearly to the breathing flow rate due to the linear dependency of the Stokes number to the air velocity (see equation (1)). Consequently, the LIF gradient follows the rise and decrease of the breathing flow rate which results in a local peak. The gradient maxima are incrementally shifted to later time-steps which can be attributed to the later arrival of aerosol at subsequent bifurcations. The aerosols follow the inhalation flow through the airway model from the ETA to the distal airways and start impacting subsequently at the bifurcations.

The rising and decreasing gradient behavior resulting in a distinct peak is not apparent for B6 to B8. In these bifurcations the gradient increases slowly and transitions immediately over to a constant gradient around the maximum value (com. Fig. 5D dashed boxes). This gradient behavior is explained by the exponential decreasing breathing flow rate at each bifurcation by flow division. This leads to a drop of breathing flow rate from the first to last airway generation by a factor of 10^7 (Möller et al., 2021), resulting in a reduced influence of inertial impaction which is linearly correlated to the breathing velocity ($St_i \sim U_i$). Additionally, larger aerosols are impacted and filtered out in the previous bifurcations due to large Stokes numbers ($St_i \sim d_p^2$) while smaller aerosols reaching B6 to B8 have better flow tracing abilities and are less prone to impaction. All these factors are expected to result in a progressively reduced deposition efficiency by inertial impaction at higher bifurcation numbers, represented by a slower increase in LIF intensity, a less distinct peak or even the absence of a peak in the LIF gradient.

At low respiratory flow rates, i.e. during breathing pauses, a linear increase in LIF intensity in Fig. 5C or a constant and positive LIF gradient in Fig. 5D is observed, indicating gravitational settling of aerosols with a constant settling velocity. The gravitational settling is apparent in all bifurcations, but the settling time decreases with higher bifurcations represented by shorter times of the linear slopes in LIF intensity or constant LIF gradients. This is explained by smaller traveling distances of the settling aerosol due to smaller airway diameters with higher generation numbers. Due to the normalization of the LIF signal in Fig. 5C the constant gradient appears larger for higher bifurcation numbers.

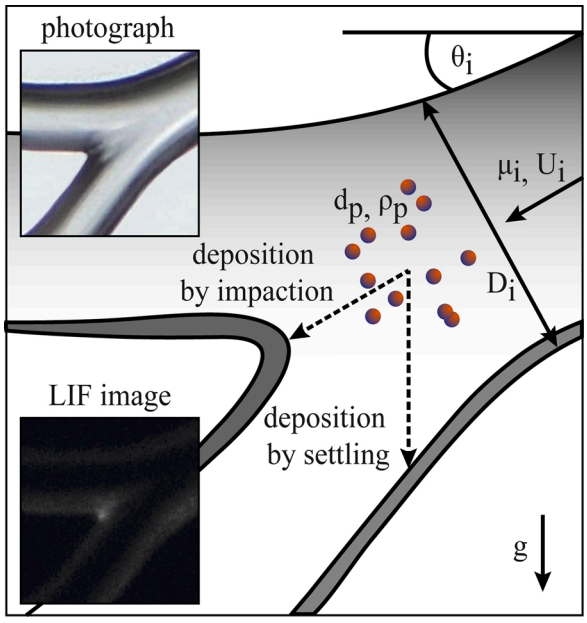

Fig. 6. Main deposition mechanisms in the upper airways and their influencing parameters.

Overall, the behavior of intensity curves in B1 to B8 can be explained by the two deposition mechanisms i) inertial impaction at higher respiratory flow rates and ii) gravitational settling at lower to zero respiratory flow rates. For these deposition mechanisms, all relevant parameters of the lung geometry and the breathing flow are summarized in Fig. 6. A decreasing influence of inertial impaction is seen over the bifurcations whereas the gravitational settling is observed in all bifurcations.

However, the resulting deposition field is dependent on the configuration of the current set-up such as the evaporation of aerosols in a dry airway model, the chosen respiratory cycle and the planar configuration of the airway geometry. These influences of the current set-up on aerosol deposition and the physiological interpretability of the measurements are discussed in section 3.5.

3.3. Comparison of the aerosol deposition to the calculated inertial impaction probability

Based on Chan and Lippman (Chan & Lippmann, 1980) a probability of inertial impaction for different sizes of aerosols is calculated for each airway generation i with

$$P_i = 1.606\, St_i + 0.0023 \tag{4}$$

The empirical formula of Chan and Lippmann (Chan & Lippmann, 1980; The Mechanics of Inhaled Pharmaceutical Aerosols, 2001) is based on experiments in casts of airways with constant breathing flows and include the effect of the larynx. According to Finlay et al. (The Mechanics of Inhaled Pharmaceutical Aerosols, 2001) the formula of Chan and Lippmann (Chan & Lippmann, 1980) represents an average of several other existing impaction probability calculations in literature.

This formula can be applied on the measured droplet size distribution of the nebulizer leading to the estimation of new droplet size distributions after impaction in each airway. For each bin of the droplet size distribution, the number of impacted aerosols can be estimated by multiplying the impaction probability and with the number of aerosols. These impacted aerosols are removed from the droplet size distribution and a new Sauter diameter D_{32} and arithmetic diameter D_{10} can be derived. The impaction probability is calculated with the maximum breathing velocity in each airway. This procedure is iteratively repeated for each airway. Thus, each ROI represents a bifurcation consisting of two airway generations, an average of the resulting mean diameter D_{32} and D_{10} of the parent and the daughter airway is taken for each bifurcation. For this deterministic calculation method, the number of aerosols in each bin needed to be increased by a factor of 1000 which doesn't change the characteristics of the droplet size distribution. Otherwise, this calculation method of multiplying the number of aerosols in each bin with the impaction probability would lead to non-impacting aerosols for bins with very low aerosol quantities.

As shown in Fig. 7A the impaction probability varies much over the generations due to high Stokes numbers in the generations from the trachea (G0) to G8 with a maximum in G5. The impaction probability is influenced by the squared diameter of the aerosols. The Sauter mean diameter D_{32} (originally 14.58 µm after nebulizing) in Fig. 7B decreases strongly between B1 to B8 with the highest gradient at B1 and a transition to a lower gradient in B8. Beyond B8 the Sauter diameter continues to decrease more slowly. The Sauter diameter represents the volume to surface area ratio of a droplet size distribution and is highly influenced by larger aerosol diameter due to their large volume to surface ratio. The arithmetic mean diameter D_{10} decreases from B1 to B24, with a particularly higher degree of D_{10} reduction between B1 to B8 and B12 to B16. The higher gradients in both D_{10} and D_{32} are correlating to the higher levels of impaction probability in Fig. 7A.

Despite of the maximum impaction probability in G5, the D_{32} shows the highest gradient at B1 and a decreasing gradient until B8. This is explained by filtering out larger aerosol sizes over the upper airway geometry which leads to the decreasing distinct peaks in the LIF gradient over the bifurcations B1 to B5 in Fig. 5D. This corresponds well to the stronger decrease of the Sauter diameter from B1 to B5 in Fig. 7B. The bifurcations B6 to B8 do not exhibit a distinct peak in the LIF intensity gradient. However, the rise of the LIF intensity in these bifurcations may still be influenced by inertial impaction since the D_{32} is still decreasing but with a lower gradient.

In comparison. The arithmetic diameter D_{10} decreases from B1 to B8 with an almost constant gradient. The droplet size distribution of a nebulizer is a right-skewed distribution (comp to Fig. 2A). Thus, small aerosol sizes with high quantities are influencing the D_{10}. Therefore, the constant drop of D_{10} from B1 to B8 shows that not only larger aerosol sizes, as seen in the curve behavior of D_{32}, but also smaller aerosol sizes (with high frequencies in the droplet size distribution) are impacting due to inertia in the bifurcations B1 to B8.

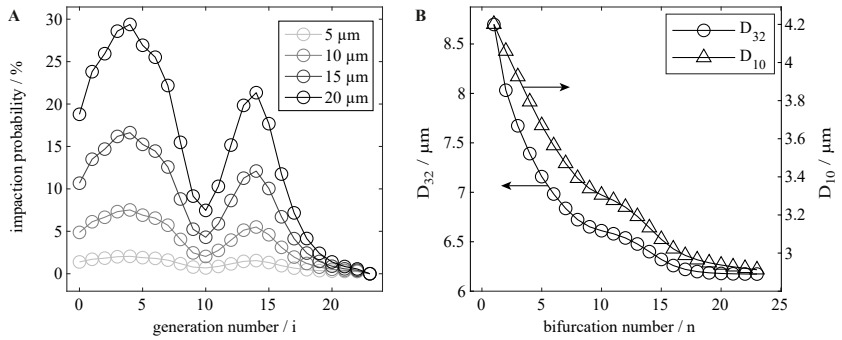

Fig. 7. A: The impaction probability over generation number and aerosol sizes. B: Influence of inertial impaction on the arithmetic and Sauter mean diameter over bifurcation number. Calculation is based on Chan and Lippmann (Chan & Lippmann, 1980).

The behavior of D_{10} is an indicator that the aerosol deposition in B6 to B8 may be affected by inertial impaction of smaller aerosol sizes. The impaction of smaller aerosol sizes may not lead to a peak in the LIF gradient due to smaller droplet volumes containing the fluorescent tracer.

In this comparison of the probability of inertial impaction based on Chan and Lippmann (Chan & Lippmann, 1980) to the LIF intensity curves in the airway model must be noted, that both models are based on different lung geometries and different breathing curves (constant vs. sinusoidal breathing curves). Further, the impaction probability is calculated based on the maximum velocity of the breathing cycle in each airway. Therefore, this calculation represents solely an estimation of the influence of inertial impaction on the droplet size distribution.

3.4. Identification of deposition mechanisms by dimensionless numbers and settling time

As shown in Fig. 5C and D the deposition behavior in the bifurcations varies with the dominant deposition mechanisms during different phases in the breathing cycle. However, the transition between both deposition mechanisms cannot be determined by the LIF deposition analysis alone. Therefore, the LIF results are discussed below based on dimensionless numbers. The Stokes number and the sedimentation parameter cannot be used due to their dependency on aerosol diameter which changes throughout the airway model by inertial impaction as discussed in the previous section and the evaporation in a dry airway model (discussed in section 3.5.1.). Therefore, the squared Froude number Fr_i^2 is introduced:

$$\mathrm{Fr_i}2 = \mathrm{St_i} \;/\; \left(\mathrm{v_{settling}} \;/\; \mathrm{U_i}\right) = \mathrm{U_i^2} \;/\; \left(\mathrm{g}\cos(\theta)\,\mathrm{D_i}\right) \tag{6}$$

The squared Froude number is the relation between the Stokes number and the non-dimensional settling number and does not depend on the aerosol diameter. It gives an indication on the dominant deposition mechanism: large Froude numbers correlate to inertial impaction whereas low Froude numbers correspond to gravitational settling. The airway inclination (angle to the horizontal) is added to the formula which is relevant for the sedimentation mechanism (Piglione et al., 2012). For a better readability the dimensionless number Fr^2 is called "Froude number" without "squared" in the following section. For calculating the Froude number in each bifurcation, an average of the corresponding Froude numbers of the airway generations is taken. For B1 a Froude number cannot be derived, since the trachea is vertically aligned, resulting in $\cos 90^\circ = 0$ in the denominator.

In addition to the dimensionless Froude number, the settling time scale is estimated for each bifurcation to verify the constant behavior of the LIF gradients during low respiratory flow rates which is considered to represent the gravitational settling of the aerosols

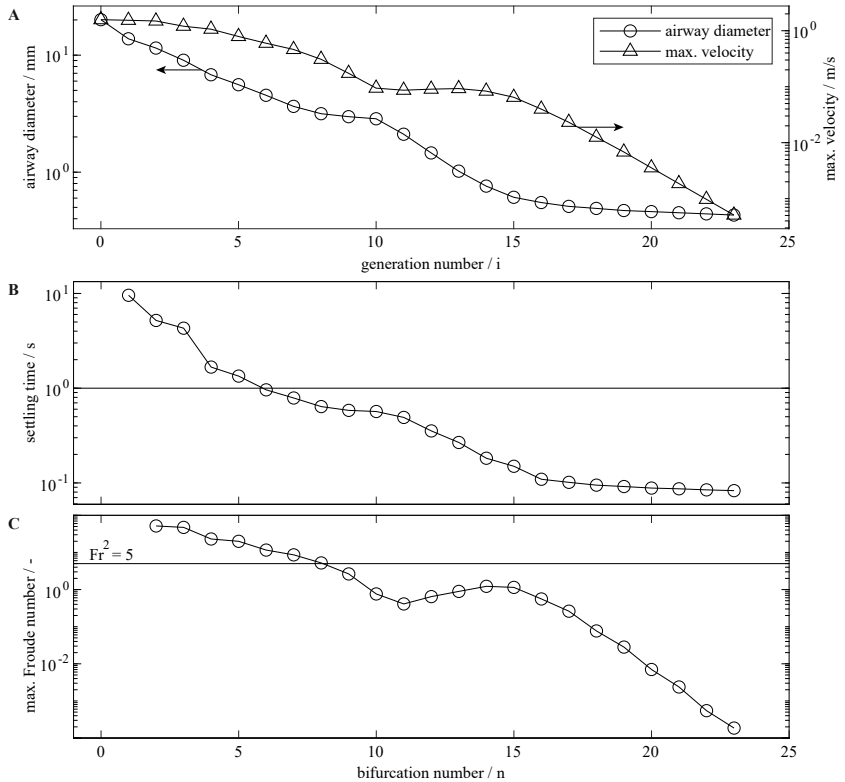

Fig. 8. A: Maximum velocity in airway and airway diameter over generations. B: Settling time of aerosols over bifurcations based on measured Sauter mean diameter D_{32}. C: Maximum squared Froude number over bifurcations, calculated with the maximum breathing velocity.

(comp. to section 3.2.). The settling time is calculated as

$$t_{settling,i} = h_i \;/\; v_{settling} = D_i \;/\; \left(v_{settling} \cos \theta_i\right) \tag{5}$$

with $v_{settling}$ from formula (3) and the implementation of the airway angle θ_i. For the trachea the settling height h_i is chosen to be the length of the airway (Möller et al., 2021) because of the term cos θ turning to zero. For deriving the settling time of the bifurcation, the settling times of the adjacent parent and daughter airway are averaged. The settling velocity $v_{settling}$ is dependent on the squared aerosol diameter. However, the measured Sauter mean diameter $D_{32} = 14.58$ µm is used for estimating the settling time. The D_{32} represents 40 % of the volume of the spray and due to its relation to the volume-to-surface area of a spray it corresponds well to the weight-to-drag force which is responsible for a constant settling velocity and for the inertial drag force governing the impaction (Casas et al., 2019). Note that the evaporation at the inlet of the ETA leads to an increased Sauter diameter as discussed in section 3.5.1. whereas the inertial impaction leads to a decreased Sauter diameter. Due to these uncertainties the calculated settling time serves only as an estimation and may only indicate trends over the bifurcations. Further, the settling time scales are estimated assuming no air flow in the airway. The settling time is applied in Fig. 9 to indicate the settling of aerosols during the constantly increasing LIF intensity after $Fr = 5$. The assumption of no flow during gravitational settling is suitable for $Fr \leq 5$ where the breathing flow in the airways is sufficiently low due to $Fr \sim U^2$ and settling starts in near-wall regions due to low local velocities and Froude numbers (Nicolaou, 2018).

Fig. 8 shows the airway diameter and the maximum velocity in each airway with the corresponding settling time and the Froude number over bifurcation number n. The airway diameter and the maximum inhalation flow rates are important parameters for the Froude ($Fr_i^2 \sim U_i^2/D_i$) and for the settling time ($t_{settling} \sim D_i$) and are therefore shown in this graph. The airway diameter in Fig. 8A decreases over generations but shows a small plateau around G8 to G10. The settling time in Fig. 8B shows a decreasing behavior over the bifurcations as a result of the decreasing airway diameter as seen in Fig. 8A. The decreasing settling time is also seen in the normalized LIF intensity in Fig. 5C and in Fig. 5D: Due to the constant settling velocity, the regime of gravitational settling is represented by a linear increase in LIF intensity and a constant, positive LIF gradient during low flow rates. Correspondingly to the decreasing settling times, the maximum normalized LIF intensity is reached earlier and the constant LIF gradient time becomes shorter

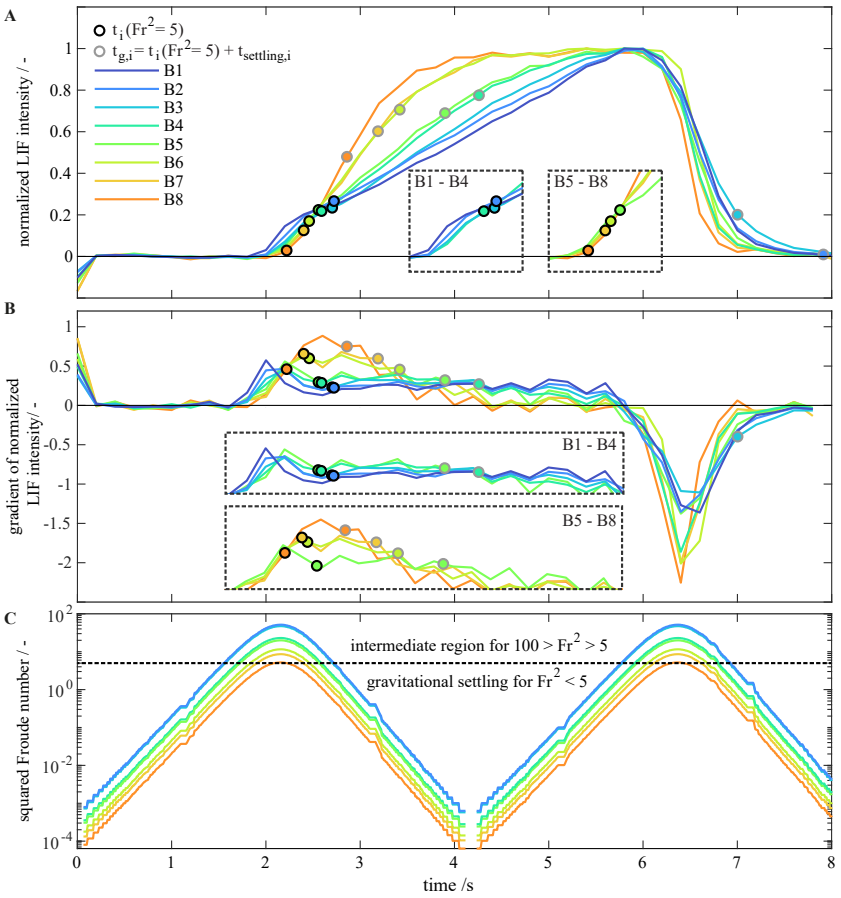

Fig. 9. A: Normalized LIF intensity from B1 to B8 over time with indication of the end of impaction t_i ($Fr^2 = 5$) (black outlined circles) and the expected end of settling $t_{g,i}$ (grey outlined circles). B: Gradient of normalized LIF intensity from B1 to B8 with indication of the end of impaction t_i ($Fr^2 = 5$) (black outlined circles) and the expected end of settling $t_{g,i}$ (grey outlined circles). C: The temporal evolution of the Froude number Fr^2 over time with indication of the aerosol deposition regimes by Piglione et al. (Piglione et al., 2012).

for higher bifurcation numbers.

For B1 to B3 the estimated settling time is greater than 4s which is longer than the time between the start of aerosol deposition and the evaporation during exhalation (comp. Fig. 5) and drops for B4 to B8 below 2 s. This drop in settling time is also represented in the LIF measurement; For B1 to B3 the LIF intensity increases nearly linearly to the maximum LIF value whereas for B4 to B8 the maximum value is successively reached at earlier times.

In Fig. 8C the maximum Froude number (calculated with the maximum mean breathing velocity in each airway) shows a decreasing behavior from B2 to B11 and also from B15 to B23. In between, from B11 to B15, the Froude number slightly increases. This behavior of the Froude number over bifurcations fits well to the literature (The Mechanics of Inhaled Pharmaceutical Aerosols, 2001) and is strongly dependent on the velocity in each airway as seen in Fig. 8A. According to Piglione et al. (Piglione et al., 2012) inertial impaction dominates for $Fr^2 > 100$, an intermediate regime is present between $100 > Fr^2 > 5$, and gravitational settling dominates for $Fr^2 < 5$. For the given airway model, the Froude number is greater than 5 for B1 to B8, meaning that for the highest inhalation flow rate, the investigated bifurcations in this study lie within the intermediate regime with both deposition mechanisms, inertial impaction and gravitational settling, being relevant. Consequently, although no clear peak is visible in the LIF gradients from B6 to B8, the aerosol deposition may be influenced by inertial impaction for high flow rates. It should be noted that the influence of the inertial impaction varies within the intermediate regime proposed by Piglione et al. (Piglione et al., 2012) and increases with higher Froude number. However, a temporal Froude number over the breathing cycle is needed to correlate the time-specific aerosol deposition within the airway model to the different deposition mechanisms.

In Fig. 9 the LIF intensity and gradient is compared to the temporal Froude number over time for the respective breathing cycle. The squared Froude number changes over several orders of magnitude over the breathing cycle due to the dependency on the breathing velocity. The LIF intensities and gradients in each bifurcation are highlighted for the time at $Fr_i^2 = 5$ in order to identify the potential transition between the intermediate regime and the gravitational settling regime in the LIF intensity curves. Further, the regime border of $Fr_i^2 = 5$ serves as the assumed zero point for the start of the settling time. The calculated settling time from Fig. 8B is added to the time t_i $(Fr_i^2 = 5)$ in order to indicate the potential end of gravitational settling regime for each bifurcation.

The transition from B2 to B5 is well characterized by the regime threshold based on the Froude number by Piglione et al. (Piglione et al., 2012). The LIF intensities and gradients from B2 to B5 are divided by $Fr_i^2 = 5$ into the intermediate region on the left of the regime border and the gravitational settling regime on the right. During the intermediate regime the LIF gradient shows a local peak which indicates the inertial impaction. No indications for gravitational settling are seen in this region, but they could be superimposed by the aerosol deposition and the resulting LIF intensity caused by inertial impaction. For $Fr_i^2 < 5$ a constant LIF gradient is apparent due to a constant settling velocity which fits well to the gravitational regime.

The LIF gradients from B6 to B8 show no local peak during the intermediate Froude regime. However, inertial impaction may still be dominant in this region. As explained above, larger aerosols are deposited and filtered out in previous bifurcations due to inertial impaction, as explained by the Sauter mean diameter D_{32} in Fig. 7B. The impaction of the smaller sized aerosols may lead to no visible peak in the LIF gradient of B6 to B8 due to the smaller volumes of the impacting aerosols containing the fluorescent tracer. Also, the duration of $Fr^2 > 5$ is much shorter for B6 to B8 than for B1 to B5. Further B6 to B8 do not experience high velocity gradients for $Fr^2 > 5$ and hence, no distinct peak can be developed in the LIF gradient.

The end of the gravitational settling $t_{g,i}$, calculated by $t_i\,({Fr_i}^2 = 5) + t_{settling,I}$, is approximated by the settling time based on a constant D_{32}. Despite of this simplification, the calculated end of gravitational settling fits relatively well to the measured data: During the proposed gravitational settling regime between $t_i\,({Fr_i}^2 = 5)$ and $t_{g,i}$ a linear increase in LIF intensity and a corresponding constant LIF gradient is seen for B2 to B7. For B8 the LIF intensity behaves not linear at the beginning of the gravitational settling regime. However, the start of gravitational settling at $Fr_i^2 = 5$ may interfere with the arrival of the first inhaled aerosols or the threshold of ${Fr_i}^2 = 5$ might not fitting to this bifurcation. A slightly smaller Froude number as threshold between intermediate and settling region would lead to a shift of t_i $(Fr_i^2 = 5)$ to the right where a linear increase of LIF signal in B8 is apparent.

After $t_{g,i}$, the end of the gravitational settling time, the LIF gradient of B4 to B8 decreases slowly to zero, leading to the conclusion that the settling of the majority of aerosols has ended. Eventually, smaller droplets containing less tracer quantities may still be settling in this region due to larger settling times (proportional to d^2) but their deposition may not be captured in the LIF images. For B8 the LIF intensity appears to be linear for a short duration after $t_{g,i}$ and the proposed end of gravitational settling does not fit perfectly to this bifurcation. The reason for this is either the false zero point with $t_i\,({Fr_i}^2 = 5)$ or the estimation of the settling time based on a constant D_{32}. The inertial impaction in the previous bifurcations could lead to a decreased D_{32} and hence, to a longer settling time. For B1 to B3 the end of settling time $t_{g,i}$ exceeds the beginning of evaporation during the exhalation and therefore a linear behavior of LIF intensity and a constant LIF gradient is seen between $t_{g,i}$ $({Fr_i}^2 = 5)$ and $t = 5.8\ s$.

Overall, the proposed definition of aerosol deposition regimes by Piglione et al. (Piglione et al., 2012) and the estimated settling time corresponds well to the measured LIF intensity of the bifurcations in the airway model.

3.5. Physiological interpretability of aerosol deposition in the current set-up

As shown in the previous sections, the 23-generation airway model enables an optical investigation of aerosol deposition by laser-induced fluorescence. For this purpose, the model offers a high optical quality of the airway surface and good optical access. In contrast to alternative models with ex-situ measurement methods and mostly steady flow rates (see Introduction), it enables an in-situ investigation of aerosol flow in air (Möller) and subsequent aerosol deposition over transient respiration. The in-situ measurement method allows the temporal and spatial analysis of aerosol flow and deposition and thereby the temporal differentiation of the relevant deposition mechanisms within the respiratory cycle.

Furthermore, the given configuration of the lung model opens up investigation possibilities that go beyond the methods used in this study; Due to the implementation of all airway generations the aerosol deposition can be analyzed in a holistic way from the trachea to the alveolar ducts. Microscopic analysis can be performed at specific positions along the airway due to the high optical quality of the airway model. Because of the adjustable breathing flow in every generation impaired flow-volume curves or flow distributions of unhealthy subjects as in the cases of ARDS or COPD can be simulated. The combination of a simplified airway geometry with well-defined boundary conditions up to the 23rd generation opens up new possibilities for the further development and validation of numerical models, requiring complementary investigations on the experimental and numerical side (CFD). Further, the airway model enables experimental comparison and development of various inhalation devices and other drug delivery methods such as instillation or bronchoscopic spraying under identical boundary conditions. The newly developed method of bronchoscopic spraying for the delivery of stem cells into the human lung has been developed and tested in this airway model (Gürzing et al., 2022). Thus, the airway model can serve as a fast testing tool of drug delivery devices over various inhalation scenarios with different breathing maneuvers and lung positions due to the high adaptability of the airway model (adjustable respiratory cycle and rotatable model position in all directions). Deposition efficiencies and fractions can be derived in future by the direct correlation of the LIF signal to the mass of the fluorescent tracer. Overall, the set-up of the airway model can contribute to the general understanding of the deposition dynamics and mechanisms of different drug delivery methods.

However, this study provides proof-of-concept for the in-situ visualization of the temporal and spatial aerosol deposition in the airway model. The airway model in its current form makes use of a number of simplifications which results inevitably in model limitations. Some of these simplifications are unavoidable for the selected design approach, others can still be eliminated and optimized in further developed model generations. Due to the chosen simplifications of the airway model, the physiological interpretability of the measured aerosol deposition in the current set-up is discussed below. This includes the currently unregulated air humidity of the inhaled air in a dry airway model, the current respiratory cycle, the planar bifurcations and the missing lung compliance.

3.5.1. Influence of the current unregulated humidity on aerosol deposition

Unlike the human lung, the airway model is not capable of self-moistening due to its dry walls. The inhaled and exhaled air into the airway model is not regulated to physiological conditions in the human lung (99.5 % RH and 37 °C) (Ferron et al., 1988). The low relative humidity of the inhaled air, the lower air temperature and the dry airway walls of the airway model can affect the evaporation of the aerosols and consequently their size. Hence, the outcoming deposition field might not be fully physiological in comparison to the deposition in the human lung. Therefore, the physiological interpretability of the aerosol deposition due to evaporation needs to be assessed.

In the set-up a mist of aerosols (D_{10} = 4.43 µm, D_{32} = 14.58 µm) is produced by the jet nebulizer which enters the airway model together with ambient air. Within the jet nebulizer reservoir, the outflowing air reaches a saturated state due to the rapid evaporation at the interface of the numerous aerosols and due to air cooling through the needed latent heat for evaporation (Dennis, 2007; Haddrell et al., 2014; Nerbrink et al., 2003; Zhou et al., 2007). The aerosol stream of the jet nebulizer and the ambient air meet in the small gap between the ETA and the outlet of the jet nebulizer (comp. to Fig. 1B) and are inhaled into the ETA of the airway model. During mixing the relative humidity decreases and an immediate evaporation of the droplets takes place depending on the relative humidity and temperature of the ambient air leading to smaller droplet sizes (Dennis, 2007; Haddrell et al., 2014; Nerbrink et al., 2003; Protheroe & Al-Jumaily, 2017; Protheroe et al., 2013; Zhou et al., 2007).

According to Protheroe et al. the streaming mixture of aerosols and air in a duct can be considered as a moving plug. Depending on the air-water-ratio in this plug either all droplets evaporate, or the rapid evaporation of aerosols increase the RH until saturation which prevents the evaporation of the remaining aerosols (Protheroe & Al-Jumaily, 2017). Protheroe et al. (Protheroe et al., 2013) demonstrate in numerical simulations the rapid temporal process of droplet evaporation while streaming through a duct; monodisperse water droplets of 5 µm (0.2 mL/min) are suspended to an air stream in a duct with a flow rate of 0.5 L/s at the temperature of 20 °C and 40 % RH. In the simulation a stable air saturation is reached after 0.13 s and the aerosol size drops from 5 µm to 3.8 µm. The

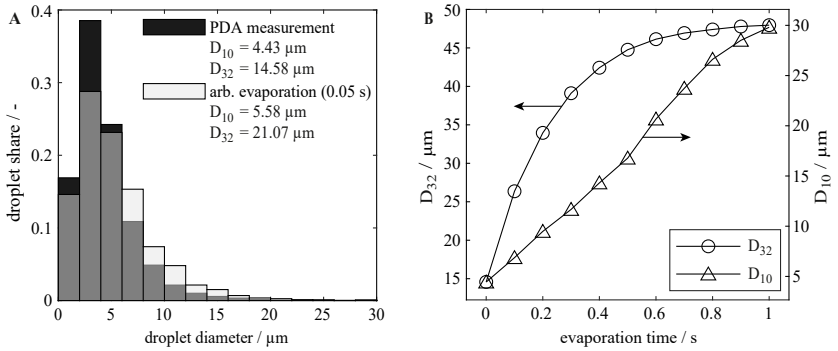

Fig. 10. A: Measured droplet size distribution of the jet nebulizer by Möller et al. (Möller et al., 2021) and a calculated droplet size distribution after an evaporation time of 0.05 s. B: Influence of evaporation time on the arithmetic and Sauter mean diameter of the droplet size distribution of the jet nebulizer based on Ferron1990 (Ferron & Soderholm, 1990).

conditions of the simulation are close to this study; the jet nebulizer produces a constant aerosol stream with a mass flow rate of 0.19 mL/min and is mixed with the ambient air of the laboratory (21 °C, estimated 40–60 % RH) with volume flow rates between 0 and 0.5 L/s. Since a minimum of 0.13 mL/min of aerosol flow rate is needed for the saturation of an air volume flow of 0.5 L/s at 40 % RH and 20 °C (Protheroe et al., 2013), a saturated state of the inhaled aerosol-air plug in the airway model is expected, even for the highest breathing flow rates of 0.5 L/s in this study. Further, the inhaled aerosols are polydisperse which may lead to a faster evaporation and saturation of the air due to the faster evaporation of the smallest aerosols in the size distribution according to the D^2 law. The D^2 law is a simplified theory on droplet evaporation and describes the proportionality of a droplet's lifetime to the square of the droplet diameter (Fei et al., 2022). This confirms that an initial and rapid evaporation takes place while the aerosol stream enters the ETA and a saturated state in the moving aerosol stream is reached fast. The visible aerosol deposition in Fig. 5 and the long travel time of 1.8 s to the first bifurcation underline that a saturated state is developed before the aerosols deposit in the first bifurcation of the airway model.

In order to verify the relevance of evaporation on the droplet size distribution and the resulting deposition behavior a simple mathematical estimate is carried out. Fig. 10A shows the droplet size distribution measured by the phase doppler technique in Möller et al. (Möller et al., 2021) and the influence of evaporation on the droplet size distribution and on the mean diameters such as D_{10} and D_{32}. A simplified evaporation of droplets is calculated based on Ferron et al. (Ferron & Soderholm, 1990) after an evaporation time of 0.05 s at 20 °C and constant 50 % RH. This short evaporation time is arbitrarily chosen and no interaction between evaporation and rise of relative humidity in the surrounding is considered. Similar to the results in Protheroe et al. (Protheroe & Al-Jumaily, 2017), the share of small droplets diminishes whereas the share of larger droplets increases due to the normalization to 100 %. Both the arithmetic diameter D_{10} and the Sauter diameter D_{32} increase from 4.43 µm to 14.58 µm–5.58 µm and 21.07 µm, respectively.

In Fig. 10B the mean diameter D_{10} and D_{32} are shown over evaporation time. Both mean diameters increase over the evaporation time with a change of 330 % for D_{32} and 670 % for D_{10} at 1 s. After this evaporation time the mean diameters decrease slowly again (not shown). The D^2 law as also used in the formula by Ferron et al. (Ferron & Soderholm, 1990) leads to the counterintuitive increase of the mean diameter of the droplet size distribution due to faster evaporation of small aerosol sizes. Overall, Figs. 10A and B shows that the evaporation has a high influence on the droplet size distribution of the jet nebulizer, especially on the smaller aerosol sizes.

Similar to the human lung a saturated state is reached rapidly at the inlet of the airway model despite the non-regulated inhaled air in a dry airway model. The initial evaporation has greater impact on smaller aerosol sizes compared to larger aerosol sizes. Due to the unknown relative humidity of the inhaled air the influence on the aerosol size distribution cannot be reconstructed. However, the visualized deposition pattern is primarily influenced by larger aerosols with high volumes and tracer content which are less affected by the evaporation.

In a self-moistening human lung an almost saturated state of 99.5 % RH is reached beyond the tracheobronchial region and is accompanied by a temperature rise to 37 °C. However, due to the missing self-moistening capability of the dry airway model the aerosols may have evaporated to a greater extent than compared to the application in the human lung. Therefore, the implementation of a humidity control for RH saturation of the air is necessary in future for preventing the excessive aerosol evaporation and for controlling the inhaled droplet size distribution within the airway model. This leads to more accurate calculations of settling times, Stokes number, sedimentation parameter and increases the interpretability and comparability to other studies using these deposition parameters for interpretation. Despite that a certain evaporation of the generated aerosols in the nebulizer during mixing with the ambient air is even realistic during the applications of jet nebulizer on humans and must be taken into account in future studies as well (Dennis, 2007; Haddrell et al., 2014; Nerbrink et al., 2003; Zhou et al., 2007). Further, the prevention of the current evaporation during exhalation may lead to the potential visualization of aerosol deposition during exhalation.

3.5.2. *Influence of the current respiratory cycle on the aerosol deposition*

The current respiratory cycle for tidal breathing is derived by the simplified sinusoidal shape of the flow-volume curve between the physiological values of tidal volume (0.5 L) and maximum flow rate (0.5 L/s) (Kleinstreuer et al., 2007; Larsen, 2016; Möller et al., 2021; Westhoff & Rühle, 2011). The sinusoidal shape of the flow-volume curve leads to the respiratory flow rate over time as shown in Fig. 5B. The resulting transient flow rate shows significant portions of low to zero flow rates and an extended mean inspiration time of 4.17 ± 0.026 s with a low breathing frequency of 7.2 breaths per minute compared to the physiological tidal breathing frequency of 12–20 breaths per minute (Larsen, 2016). Due to the non-physiological predominance of low air velocities at the beginning and end of the inhalation and expiration, the deposition mechanism of gravitational settling is overrepresented in comparison to a more physiological respiration. However, the extended times of low flow rates in this study support the identification of the deposition mechanisms from the evaluated LIF intensities and showed the depletion of aerosols by gravitational settling due to the decreasing settling times in distal bifurcations (comp. to Fig. 9). In future, a more physiological flow-volume curve for tidal breathing should be implemented in the airway model by adapting the flow-volume curve of the programmable volume flow control to a more physiological shape (Behnia & Sietsema, 2023; Chambers et al., 2019; Criée et al., 2015; Schmalisch et al., 2005).

3.5.3. *Influence of planar bifurcations on the aerosol deposition*

To ensure the best possible optical access to the airways, the model in its current configuration is chosen to be planar with symmetrical bifurcations. It is known that a planar configuration can result in a different flow profile than a more physiological off-plane configuration, i.e. with regard to the volume flow distribution and the formation of secondary flows (Comer et al., 2000; Kim & Fisher, 1999; Kleinstreuer & Zhang, 2009; Liu et al., 2002). According to Liu et al. (Liu et al., 2002) an in-plane bifurcation model leads to an imbalance of the flow distribution at the bifurcations compared to off-plane models. In the airway model, the flow distribution at each bifurcation is imposed by the adjustable rotameters for each generation, overcoming the potential imbalance in planar models. However, secondary flows may be altered which influence the local aerosol deposition.

In order to quantify the influence of this simplification, the model should be supplemented in future with further model configurations including off-plane bifurcations. However, starting with a planar configuration offers a sensible way of gradually increasing the complexity of the problem. The present modeling concept (i.e. based on an airway with generation-specific volume flow imposition) naturally offers the possibility of realizing further models with alternative geometries in near future – e. g. smooth geometries or patient-specific geometries based on CT data.

3.5.4. Influence of rigid walls of the airway model on the aerosol deposition

Due to the manufacturing of the airway model in quartz glass for ensuring the high surface quality for optical in-situ measurement methods the airway model is rigid and cannot display the expansion and contraction of the human lung during respiration. This unavoidable simplification needs to be considered especially in the distal airways starting from the respiratory bronchioles where alveoli are embedded to the walls of the alveolar ducts (G16 – G23). But also the minor motion in the upper airways influences the flow characteristics and aerosol deposition in the airways according to Mead-Hunter et al. (Mead-Hunter et al., 2013). According to numerical simulations the wall motion of the alveoli and alveolar ducts during breathing affects the aerosol deposition of mainly sub-micron particles due to local convective flows (Darquenne et al., 2009; Haber et al., 2003; Hofemeier & Sznitman, 2016; Li et al., 2023). The influence of moving walls on aerosol deposition are partially contradicting in literature with a proposed increased aerosol deposition within a moving alveolus or an alveolar duct model (C. Darquenne et al., 2009; Haber et al., 2003), or a suggested decreased aerosol deposition in a moving acinar model (Li et al., 2023).

However, the airway model cannot simulate the wall motion and may under- or overestimate the aerosol deposition in this region due to the missing lung compliance and the missing geometrical representation of the alveoli. The geometry of the alveoli may be added to the airway model in future studies, but the implementation of moving walls in in-vitro airway models remains difficult. Only few in-vitro studies focus on the flow field in moving acinar models using Particle Image Velocimetry (PIV) (Berg et al., 2010; Oakes et al., 2010) but no studies are found regarding the aerosol deposition in moving in-vitro models.

4. Summary and outlook

The aerosol deposition by a jet nebulizer has been visualized for the first time in the airway model using an in-situ measurement technique of laser-induced fluorescence (LIF). The temporal and spatial post-processing of resulting LIF images provides insight into the deposition behavior of aerosols in the first eight bifurcations over a transient respiratory cycle. Further, the LIF intensity and their gradient in the bifurcations B1 to B8 is correlated to the main deposition mechanisms in the conducting airways: i) the inertial impaction and ii) the gravitational settling. Inertial impaction is characterized by a visible peak in the LIF gradient during high inhalation flow rates while gravitational settling is expressed by a constant LIF gradient due to constant aerosol settling velocities during low respiratory flow rates. The observed deposition behavior matches well with the impaction deposition probability by Chan and Lippmann (Chan & Lippmann, 1980) and with the definition of aerosol deposition regimes in the human lung by Piglione et al. (Piglione et al., 2012). The threshold of $Fr_i^{\,2} = 5$ for gravitational settling combined with the estimated settling times fits well to the constantly increasing LIF intensity of settling aerosols.

This study shows the potential of the measurement system to resolve temporal and spatial aerosol deposition in the airway model. In future, it should be complemented with a relative humidity control of the inhaled air for preventing aerosol evaporation during inhalation and exhalation leading to a better prediction of aerosol sizes within the airway model.

CRediT authorship contribution statement

Stefanie Gürzing: Writing – review & editing, Writing – original draft, Visualization, Validation, Software, Project administration, Methodology, Investigation, Formal analysis, Data curation, Conceptualization. **Anja Lena Thiebes:** Supervision. **Christian Gabriel Cornelissen:** Funding acquisition. **Stefan Jockenhoevel:** Supervision. **Manuel Reddemann:** Supervision, Project administration, Funding acquisition.

Declaration of competing interest

The authors declare that they have no known competing financial interests or personal relationships that could have appeared to influence the work reported in this paper.

Acknowledgements

This project was funded by the Deutsche Forschungsgemeinschaft (DFG, German Research Foundation) - Project no. 394605884 (RE 4092/2-1).

Appendix A. Supplementary data

Supplementary data to this article can be found online at https://doi.org/10.1016/j.jaerosci.2025.106634.

Data availability

Data will be made available on request.

References

Ahookhosh, K., Pourmehran, O., Aminfar, H., Mohammadpourfard, M., Sarafraz, M. M., & Hamishehkar, H. (2020). Development of human respiratory airway models: A review. *European Journal of Pharmaceutical Sciences: Official Journal of the European Federation for Pharmaceutical Sciences, 145*, Article 105233. https://doi.org/10.1016/j.ejps.2020.105233

Artigas, A., Camprubí-Rimblas, M., Tantinyà, N., Bringué, J., Guillamat-Prats, R., & Matthay, M. A. (2017). Inhalation therapies in acute respiratory distress syndrome. *Annals of Translational Medicine, 5*(14), 293. https://doi.org/10.21037/atm.2017.07.21

Azarnoosh, J., Sreenivas, K., & Arabshahi, A. (2020). Numerical simulation of tidal breathing through the human respiratory tract. *Journal of Biomechanical Engineering, 142*(6), Article 61009.

Barjaktarevic, I. Z., & Milstone, A. P. (2020). Nebulized therapies in COPD: Past, present, and the future. *International Journal of Chronic Obstructive Pulmonary Disease, 15*, 1665–1677. https://doi.org/10.2147/COPD.S252435

Behnia, M., & Sietsema, K. E. (2023). Utility of cardiopulmonary exercise testing in chronic obstructive pulmonary disease: A review. *International Journal of Chronic Obstructive Pulmonary Disease, 18*, 2895–2910. https://doi.org/10.2147/COPD.S432841

Berg, E. J., Weisman, J. L., Oldham, M. J., & Robinson, R. J. (2010). Flow field analysis in a compliant acinus replica model using particle image velocimetry (PIV). *Journal of Biomechanics, 43*(6), 1039–1047. https://doi.org/10.1016/j.jbiomech.2009.12.019

Biddiscombe, M. F., Meah, S. N., Underwood, S. R., & Usmani, O. S. (2011). Comparing lung regions of interest in gamma scintigraphy for assessing inhaled therapeutic aerosol deposition. *Journal of Aerosol Medicine and Pulmonary Drug Delivery, 24*(3), 165–173. https://doi.org/10.1089/jamp.2010.0845

Borghardt, J. M., Kloft, C., & Sharma, A. (2018). Inhaled therapy in respiratory disease: The complex interplay of pulmonary kinetic processes. *Canadian Respiratory Journal, 2018*, Article 2732017. https://doi.org/10.1155/2018/2732017

Carvalho, T. C., Peters, J. I., & Williams, R. O. (2011). Influence of particle size on regional lung deposition–what evidence is there? *International Journal of Pharmaceutics, 406*(1–2), 1–10. https://doi.org/10.1016/j.ijpharm.2010.12.040

Casas, Y. A., Duran, J. A., Schoeggl, F. F., & Yarranton, H. W. (2019). Settling of asphaltene aggregates in n -Alkane diluted bitumen. *Energy & Fuels, 33*(11), 10687–10703. https://doi.org/10.1021/acs.energyfuels.9b02571

Chambers, D., Huang, C., & Matthews, G. (2019). *Basic physiology for anaesthetists*. Cambridge University Press. https://doi.org/10.1017/9781108565011

Chan, T. L., & Lippmann, M. (1980). Experimental measurements and empirical modelling of the regional deposition of inhaled particles in humans. *American Industrial Hygiene Association Journal, 41*(6), 399–409. https://doi.org/10.1080/15298668091424942

Chen, X., Feng, Y., Zhong, W., Sun, B., & Tao, F. (2018). Numerical investigation of particle deposition in a triple bifurcation airway due to gravitational sedimentation and inertial impaction. *Powder Technology, 323*, 284–293. https://doi.org/10.1016/j.powtec.2017.09.050

Cheng, Y. S. (2014). Mechanisms of pharmaceutical aerosol deposition in the respiratory tract. *AAPS PharmSciTech, 15*(3), 630–640. https://doi.org/10.1208/s12249-014-0092-0

Cheng, Y.-S., Zhou, Y., & Chen, B. T. (1999). Particle deposition in a cast of human oral airways. *Aerosol Science and Technology, 31*(4), 286–300. https://doi.org/10.1080/027868299304165

Comer, J. K., Kleinstreuer, C., Hyun, S., & Kim, C. S. (2000). Aerosol transport and deposition in sequentially bifurcating airways. *Journal of Biomechanical Engineering, 122*(2), 152–158. https://doi.org/10.1115/1.429636

Comer, J. K., Kleinstreuer, C., & Kim, C. S. (2001). Flow structures and particle deposition patterns in double-bifurcation airway models. Part 2. Aerosol transport and deposition. *Journal of Fluid Mechanics, 435*, 55–80. https://doi.org/10.1017/S0022112001003810

Conway, J. (2012). Lung imaging - Two dimensional gamma scintigraphy, SPECT, CT and PET. *Advanced Drug Delivery Reviews, 64*(4), 357–368. https://doi.org/10.1016/j.addr.2012.01.013

Criée, C.-P., Baur, X., Berdel, D., Bösch, D., Gappa, M., Haidl, P., Husemann, K., Jörres, R. A., Kabitz, H.-J., Kardos, P., Köhler, D., Magnussen, H., Merget, R., Mitfessel, H., Nowak, D., Ochmann, U., Schürmann, W., Smith, H.-J., Sorichter, S., … Worth, H. (2015). Leitlinie zur Spirometrie. Leitlinie der Deutschen Atemwegsliga, der Deutschen Gesellschaft für Pneumologie und Beatmungsmedizin und der Deutschen Gesellschaft für Arbeitsmedizin und Umweltmedizin zur Spirometrie. *Pneumologie, 69*(3), 147–164. https://doi.org/10.1055/s-0034-1391345 [Standardization of spirometry: 2015 update. Published by German Atemwegsliga, German Respiratory Society and German Society of Occupational and Environmental Medicine].

Darquenne, C. (2012). Aerosol deposition in health and disease. *Journal of Aerosol Medicine and Pulmonary Drug Delivery, 25*(3), 140–147. https://doi.org/10.1089/jamp.2011.0916

Darquenne, C., Harrington, L., & Prisk, G. K. (2009). Alveolar duct expansion greatly enhances aerosol deposition: A three-dimensional computational fluid dynamics study. *Philosophical Transactions. Series A, Mathematical, Physical, and Engineering Sciences, 367*(1896), 2333–2346. https://doi.org/10.1098/rsta.2008.0295

Delvadia, R., Hindle, M., Longest, P. W., & Byron, P. R. (2013). In vitro tests for aerosol deposition II: Ivivcs for different dry powder inhalers in normal adults. *Journal of Aerosol Medicine and Pulmonary Drug Delivery, 26*(3), 138–144. https://doi.org/10.1089/jamp.2012.0975

Delvadia, R. R., Longest, P. W., & Byron, P. R. (2012). In vitro tests for aerosol deposition. I: Scaling a physical model of the upper airways to predict drug deposition variation in normal humans. *Journal of Aerosol Medicine and Pulmonary Drug Delivery, 25*(1), 32–40. https://doi.org/10.1089/jamp.2011.0905

Dennis, J. H.[J. H. (2007). Nebulizer efficiency: Modeling versus in vitro testing. *Respiratory Care, 52*(8), 984–988.

Dugernier, J., Hesse, M., Vanbever, R., Depoortere, V., Roeseler, J., Michotte, J.-B., Laterre, P.-F., Jamar, F., & Reychler, G. (2017). Spect-CT comparison of lung deposition using a system combining a vibrating-mesh nebulizer with a valved holding chamber and a conventional jet nebulizer: A randomized cross-over study. *Pharmaceutical Research, 34*(2), 290–300. https://doi.org/10.1007/s11095-016-2061-7

Fei, L., Qin, F., Wang, G., Luo, K. H., Derome, D., & Carmeliet, J. (2022). Droplet evaporation in finite-size systems: Theoretical analysis and mesoscopic modeling. *Physical Review. E, 105*(2–2), Article 25101. https://doi.org/10.1103/PhysRevE.105.025101

Feng, Y., Zhao, J., Hayati, H., Sperry, T., & Yi, H. (2021). Tutorial: Understanding the transport, deposition, and translocation of particles in human respiratory systems using computational fluid-particle dynamics and physiologically based toxicokinetic models. *Journal of Aerosol Science, 151*, Article 105672. https://doi.org/10.1016/j.jaerosci.2020.105672

Ferron, G. A., Haider, B., & Kreyling, W. G. (1988). Inhalation of salt aerosol particles—I. Estimation of the temperature and relative humidity of the air in the human upper airways. *Journal of Aerosol Science, 19*(3), 343–363.

Ferron, G., & Soderholm, S. (1990). Estimation of the times for evaporation of pure water droplets and for stabilization of salt solution particles. *Journal of Aerosol Science, 21*(3), 415–429. https://doi.org/10.1016/0021-8502(90)90070-E

Fleming, J. S., Sauret, V., Conway, J. H., & Martonen, T. B. (2004). Validation of the conceptual anatomical model of the lung airway. *Journal of Aerosol Medicine: The Official Journal of the International Society for Aerosols in Medicine, 17*(3), 260–269. https://doi.org/10.1089/jam.2004.17.260

Große, S., Schröder, W., Klaas, M., Klöckner, A., & Roggenkamp, J. (2007). Time resolved analysis of steady and oscillating flow in the upper human airways. *Experiments in Fluids, 42*(6), 955–970. https://doi.org/10.1007/s00348-007-0318-y

Gürzing, S., Thiebes, A. L., Cornelissen, C. G., Jockenhoevel, S., & Reddemann, M. A. (2022). Suitability of bronchoscopic spraying for fluid deposition in lower airway regions: Fluorescence analysis on a transparent in vitro airway model. *Journal of Aerosol Medicine and Pulmonary Drug Delivery, 35*(5), 269–277. https://doi.org/10.1089/jamp.2022.0016

Haber, S., Yitzhak, D., & Tsuda, A. (2003). Gravitational deposition in a rhythmically expanding and contracting alveolus. *Journal of Applied Physiology, 95*(2), 657–671. https://doi.org/10.1152/japplphysiol.00770.2002

Haddrell, A. E., Davies, J. F., Miles, R. E. H., Reid, J. P., Dailey, L. A., & Murnane, D. (2014). Dynamics of aerosol size during inhalation: Hygroscopic growth of commercial nebulizer formulations. *International Journal of Pharmaceutics, 463*(1), 50–61. https://doi.org/10.1016/j.ijpharm.2013.12.048

Heenan, A. F., Matida, E., Pollard, A., & Finlay, W. H.[W. H. (2003). Experimental measurements and computational modeling of the flow field in an idealized human oropharynx. *Experiments in Fluids, 35*(1), 70–84.

Heistracher, T., & Hofmann, W.[W. (1995). Physiologically realistic models of bronchial airway bifurcations. *Journal of Aerosol Science, 26*(3), 497–509.

Hofemeier, P., & Sznitman, J. (2016). The role of anisotropic expansion for pulmonary acinar aerosol deposition. *Journal of Biomechanics, 49*(14), 3543–3548. https://doi.org/10.1016/j.jbiomech.2016.08.025

Hofmann, W.[W. (2020). Regional deposition: Deposition models. *Journal of Aerosol Medicine and Pulmonary Drug Delivery, 33*(5), 239–248. https://doi.org/10.1089/jamp.2020.29031.wh

Holbrook, L. T., & Longest, P. W. (2013). Validating CFD predictions of highly localized aerosol deposition in airway models: In vitro data and effects of surface properties. *Journal of Aerosol Science, 59*, 6–21. https://doi.org/10.1016/j.jaerosci.2013.01.008

Islam, M. S., Paul, G., Ong, H. X., Young, P. M., Gu, Y. T., & Saha, S. C. (2020). A review of respiratory anatomical development, air flow characterization and particle deposition. *International Journal of Environmental Research and Public Health, 17*(2). https://doi.org/10.3390/ijerph17020380

Janke, T., Koullapis, P., Kassinos, S. C., & Bauer, K.[K. (2019). Piv measurements of the SimInhale benchmark case. *European Journal of Pharmaceutical Sciences: Official Journal of the European Federation for Pharmaceutical Sciences, 133*, 183–189. https://doi.org/10.1016/j.ejps.2019.03.025

Johnstone, A., Uddin, M., Pollard, A., Heenan, A., & Finlay, W. H. (2004). The flow inside an idealised form of the human extra-thoracic airway. *Experiments in Fluids, 37*(5), 673–689.

Kim, C. S., & Fisher, D. M. (1999). Deposition characteristics of aerosol particles in sequentially bifurcating airway models. *Aerosol Science and Technology: The Journal of the American Association for Aerosol Research, 31*(2–3), 198–220. https://doi.org/10.1080/027868299304255

Kleinstreuer, C., Zhang, Z., & Kim, C. S. (2007). Combined inertial and gravitational deposition of microparticles in small model airways of a human respiratory system. *Journal of Aerosol Science, 38*(10), 1047–1061. https://doi.org/10.1016/j.jaerosci.2007.08.010

Kleinstreuer, C., & Zhang, Z. (2009). An adjustable triple-bifurcation unit model for air-particle flow simulations in human tracheobronchial airways. *Journal of Biomechanical Engineering, 131*(2), Article 21007. https://doi.org/10.1115/1.3005339

Larsen, R. (2016). Physiologie der Atmung. In R. Larsen (Ed.), *Anästhesie und Intensivmedizin für die Fachpflege* (pp. 696–708). Springer Berlin Heidelberg. https://doi.org/10.1007/978-3-662-50444-4_52.

Li, P., Guo, W., Fan, J., Su, C., Zhao, X., & Xu, X. (2023). Aerosol deposition in the pulmonary acinar region: Influence of wall motion and interparticle collisions. *Journal of Aerosol Science, 167*, Article 106077. https://doi.org/10.1016/j.jaerosci.2022.106077

Liu, Y., So, R. M. C., & Zhang, C. H. (2002). Modeling the bifurcating flow in a human lung airway. *Journal of Biomechanics, 35*(4), 465–473. https://doi.org/10.1016/S0021-9290(01)00225-1

Lizal, F., Jedelsky, J., Morgan, K., Bauer, K., Llop, J., Cossio, U., Kassinos, S., Verbanck, S., Ruiz-Cabello, J., Santos, A., & others. (2018). Experimental methods for flow and aerosol measurements in human airways and their replicas. *European Journal of Pharmaceutical Sciences, 113*, 95–131.

Longest, P. W., & Holbrook, L. T. (2012a). In silico models of aerosol delivery to the respiratory tract - Development and applications. *Advanced Drug Delivery Reviews, 64*(4), 296–311.

Longest, P. W., & Holbrook, L. T. (2012b). In silico models of aerosol delivery to the respiratory tract—development and applications. *Advanced Drug Delivery Reviews, 64*(4), 296–311.

Longest, P. W., Tian, G., Delvadia, R., & Hindle, M. (2012). Development of a stochastic individual path (SIP) model for predicting the deposition of pharmaceutical aerosols: Effects of turbulence, polydisperse aerosol size, and evaluation of multiple lung lobes. *Aerosol Science and Technology, 46*(12), 1271–1285. https://doi.org/10.1080/02786826.2012.708799

McCracken, J. L., Veeranki, S. P., Ameredes, B. T., & Calhoun, W. J. (2017). Diagnosis and management of asthma in adults: A review. *JAMA, 318*(3), 279–290. https://doi.org/10.1001/jama.2017.8372

Mead-Hunter, R., King, A. J., Larcombe, A. N., & Mullins, B. J. (2013). The influence of moving walls on respiratory aerosol deposition modelling. *Journal of Aerosol Science, 64*, 48–59. https://doi.org/10.1016/j.jaerosci.2013.05.006

The mechanics of inhaled pharmaceutical aerosols. (2001). Elsevier. https://doi.org/10.1016/B978-0-12-256971-5.X5000-7

Möller, G., Bieber, M., Gürzing, S., Thiebes, A. L., Klein, S., Cornelissen, C. G., & Reddemann, M. A. (2021). Transparent 23-generation airway model for experimental investigation of aerosol flow and deposition within the human respiratory tract. *Journal of Aerosol Science, 156*, Article 105782.

Nerbrink, O. L., Pagels, J., Pieron, C. A., & Dennis, J. H. (2003). Effect of humidity on constant output and breath enhanced nebulizer designs when tested in the EN 13544-1 EC standard. *Aerosol Science and Technology: The Journal of the American Association for Aerosol Research, 37*(3), 282–292. https://doi.org/10.1080/02786820300948

Nicolaou, L. (2018). Inertial and gravitational effects on aerosol deposition in the conducting airways. *Journal of Aerosol Science, 120*, 32–51. https://doi.org/10.1016/j.jaerosci.2018.03.003

Nordlund, M., Belka, M., Kuczaj, A. K., Lizal, F., Jedelsky, J., Elcner, J., Jicha, M., Sauser, Y., Le Bouhellec, S., Cosandey, S., Majeed, S., Vuillaume, G., Peitsch, M. C., & Hoeng, J. (2017). Multicomponent aerosol particle deposition in a realistic cast of the human upper respiratory tract. *Inhalation Toxicology, 29*(3), 113–125. https://doi.org/10.1080/08958378.2017.1315196

Oakes, J. M., Day, S., Weinstein, S. J., & Robinson, R. J. (2010). Flow field analysis in expanding healthy and emphysematous alveolar models using particle image velocimetry. *Journal of Biomechanical Engineering, 132*(2), Article 21008. https://doi.org/10.1115/1.4000870

Ou, C., Hang, J., & Deng, Q. (2020). Particle deposition in Human Lung airways: Effects of airflow, particle size, and mechanisms. *Aerosol and Air Quality Research, 20*(12), 2846–2858. https://doi.org/10.4209/aaqr.2020.02.0067

Piglione, M. C., Fontana, D., & Vanni, M. (2012). Simulation of particle deposition in human central airways. *European Journal of Mechanics - B: Fluids, 31*, 91–101. https://doi.org/10.1016/j.euromechflu.2011.08.003

Protheroe, M. D., & Al-Jumaily, A. M. (2017). Evaporation characteristics in nebuliser based humidification and drug delivery devices. *Journal of Aerosol Science, 109*, 13–27. https://doi.org/10.1016/j.jaerosci.2017.03.005

Protheroe, M. D., Al-Jumaily, A., & Nates, R. J. (2013). Prediction of droplet evaporation characteristics of nebuliser based humidification and drug delivery devices. *International Journal of Heat and Mass Transfer, 60*, 772–780. https://doi.org/10.1016/j.ijheatmasstransfer.2013.01.053

Schmalisch, G., Wilitzki, S., & Wauer, R. R. (2005). Differences in tidal breathing between infants with chronic lung diseases and healthy controls. *BMC Pediatrics, 5*, 36. https://doi.org/10.1186/1471-2431-5-36

Sera, T., Kamiya, N., Fukushima, T., & Tanaka, G. (2021). Visualizing the flow patterns in an expanding and contracting pulmonary alveolated duct based on microcomputed tomography images. *Journal of Biomechanical Engineering, 143*(7). https://doi.org/10.1115/1.4050285

Su, W.-C., & Cheng, Y. S. (2006a). Deposition of fiber in a human airway replica. *Journal of Aerosol Science, 37*(11), 1429–1441. https://doi.org/10.1016/j.jaerosci.2006.01.015

Su, W.-C., & Cheng, Y. S. (2006b). Fiber deposition pattern in two human respiratory tract replicas. *Inhalation Toxicology, 18*(10), 749–760. https://doi.org/10.1080/08958370600748513

Su, W.-C., & Cheng, Y. S. (2009). Deposition of man-made fibers in human respiratory airway casts. *Journal of Aerosol Science, 40*(3), 270–284. https://doi.org/10.1016/j.jaerosci.2008.11.003

Sznitman, J. (2013). Respiratory microflows in the pulmonary acinus. *Journal of Biomechanics, 46*(2), 284–298. https://doi.org/10.1016/j.jbiomech.2012.10.028

Tropea, C., Yarin, A., & Foss, J. F. (Eds.). (2007). *Springer handbooks*. *Springer Handbook of Experimental Fluid Mechanics*. Springer Berlin Heidelberg. http://nbn-resolving.org/urn:nbn:de:bsz:31-epflicht-1494610.

Westhoff, M., & Rühle, K.-H. (2011). Spiroergometrie. *Der Pneumologe, 8*(2), 85–91. https://doi.org/10.1007/s10405-010-0451-9

Williams, J., Ahlqvist, H., Cunningham, A., Kirby, A., Katz, I., Fleming, J., Conway, J., Cunningham, S., Ozel, A., & Wolfram, U. (2024). Validated respiratory drug deposition predictions from 2D and 3D medical images with statistical shape models and convolutional neural networks. *PLoS One, 19*(1), Article e0297437. https://doi.org/10.1371/journal.pone.0297437

Williams, J., Kolehmainen, J., Cunningham, S., Ozel, A., & Wolfram, U. (2022). Effect of patient inhalation profile and airway structure on drug deposition in image-based models with particle-particle interactions. *International Journal of Pharmaceutics, 612*, Article 121321. https://doi.org/10.1016/j.ijpharm.2021.121321

Xi, J., Talaat, M., Si, X. A., Han, P., Dong, H., & Zheng, S. (2020). Alveolar size effects on nanoparticle deposition in rhythmically expanding-contracting terminal alveolar models. *Computers in Biology and Medicine, 121*, Article 103791. https://doi.org/10.1016/j.compbiomed.2020.103791

Xu, X., Wu, J., Weng, W., & Fu, M. (2020). Investigation of inhalation and exhalation flow pattern in a realistic human upper airway model by PIV experiments and CFD simulations. *Biomechanics and Modeling in Mechanobiology, 19*(5), 1679–1695. https://doi.org/10.1007/s10237-020-01299-3

Yeh, H.-C., & Schum, G. M. (1980). Models of human lung airways and their application to inhaled particle deposition. *Bulletin of Mathematical Biology, 42*(3), 461–480.

Zeng, X. M., Martin, G. P., & Marriott, C. (2000). *Particulate interactions in dry powder formulations for inhalation*. CRC Press. https://doi.org/10.3109/9780203209592

Zhang, Y., & Finlay, W. H. (2005). Experimental measurements of particle deposition in three proximal lung bifurcation models with an idealized mouth-throat. *Journal of Aerosol Medicine: The Official Journal of the International Society for Aerosols in Medicine, 18*(4), 460–473. https://doi.org/10.1089/jam.2005.18.460

Zhou, Y., Brasel, T. L., Kracko, D., Cheng, Y.-S., Ahuja, A., Norenberg, J. P., & Kelly, H. W. (2007). Influence of impactor operating flow rate on particle size distribution of four jet nebulizers. *Pharmaceutical Development and Technology, 12*(4), 353–359. https://doi.org/10.1080/10837450701366937

Zhou, Y., & Cheng, Y.-S. (2005). Particle deposition in a cast of human tracheobronchial airways. *Aerosol Science and Technology, 39*(6), 492–500. https://doi.org/10.1080/027868291001385